A high level *ab initio* map and direct statistical treatment of the fragmentation of singlet ketene

Stephen J. Klippenstein
Chemistry Department, Case Western Reserve University, Cleveland, Ohio 44106-7078

Allan L. L. East[a] and Wesley D. Allen[b]
Department of Chemistry, Stanford University, Stanford, California 94305

(Received 20 December 1995; accepted 1 March 1996)

State-of-the-art *ab initio* quantum chemical techniques have been employed to ascertain the reaction path and associated energetics for the dissociation of CH_2CO into $^1CH_2+CO$ and thereby to investigate the kinetics of this dissociation via variational Rice–Ramsperger–Kassel–Marcus (RRKM) theory. The quantum chemical computations focused on the determination of geometric structures, energies, and force fields for four constrained C–C distances (2.2, 2.5, 2.8, and 3.1 Å) spanning the inner transition-state region. Optimized structures were obtained with the coupled-cluster singles and doubles method including a perturbative triples term [CCSD(T)], as implemented with a contracted [C/O, H] basis set of $[5s4p2d1f, 4s2p1d]$ quality. The resulting energetics were corrected for basis set incompleteness and higher-order electron correlation with the aid of second-order Møller–Plesset perturbation theory (MP2) predictions given by an immense $[13s8p6d4f, 8s6p4d]$ basis combined with 6–31G* Brueckner doubles results augmented with perturbative contributions from both connected triple and quadruple excitations. Quadratic force fields along the reaction path were determined at the CCSD/$[5s4p2d, 4s2p]$ level of theory. Anharmonic effects in the enumeration of accessible states for the transition state were accounted for by a direct statistics approach involving repeated MP2/6-31G* energy evaluations. Two separate reaction coordinates defined by the C–C bond length or alternatively the center-of-mass separation between the $^1CH_2$ and CO fragments were explicitly considered in these direct statistical analyses. A spectroscopic quality quartic force field for ketene derived in a companion *ab initio* study was employed in the evaluation of the anharmonic reactant density of states. The final statistical predictions for the energy dependence of the dissociation rate constant are found to be in quantitative agreement with experiment (i.e., generally within 30%), thereby providing strong evidence for the quantitative validity of variational RRKM theory. © *1996 American Institute of Physics.* [S0021-9606(96)03321-1]

I. INTRODUCTION

Rice–Ramsperger–Kassel–Marcus (RRKM) theory has long provided an important means for estimating the kinetics of dissociation reactions.[1–3] Within variational RRKM theory[4] the energy (E) and total angular momentum (J) resolved rate constant for dissociation, k_{EJ}, is given by

$$k_{EJ}=\frac{N^{\dagger}_{EJ}}{h\rho_{EJ}}, \tag{1}$$

where $N^{\dagger}_{EJ}$ is the variationally minimized number of states with energy less than or equal to E and with total angular momentum quantum number J. This number of available states is evaluated for motion restricted to a surface separating the reactant from the products, and the variational minimization is performed with respect to the definition of the surface. The particular dividing surface corresponding to this minimum is then labeled the transition state, as it provides a qualitative indication of where the transition from reactants to products occurs. The denominator ρ_{EJ} in Eq. (1) is in turn the density of states for the reactant molecule at the given energy and total angular momentum.

Numerous comparisons between the predictions of RRKM theory and experimental measurements have provided evidence for the validity of the theory.[2,3] However, for the important special case of dissociations for which the reverse recombination is barrierless, there have been very few completely nonempirical assessments of its validity. This dearth of nonempirical studies is due in part to the difficulty of accurately determining the energetics of the transition-state region. Moreover, the location of the dynamical transition state varies quite widely with energy, hindering the evaluation of its number of states even given accurate energetic estimates. Of course, a meaningful assessment of the validity of RRKM theory for these reactions also requires accurate E and J resolved experimental data for comparison. The majority of the comparisons between RRKM theory and experiment have thus involved a simple modeling of the energy and/or temperature dependence based on qualitatively realistic estimates for the underlying rovibrational energy levels, with agreement between the calculated and observed

[a]Current address: Steacie Institute for Molecular Sciences, National Research Council of Canada, Ottawa, Ontario, K1A 0R6, Canada.
[b]Current address: Center for Computational Quantum Chemistry, University of Georgia, Athens, GA 30602.

 0021-9606/96/105(1)/118/23/$10.00

energy dependence then taken as confirmation of the underlying foundations of RRKM theory.

In this article, the validity of RRKM theory is addressed for ''barrierless'' reactions at a more fundamental level. In particular, each of the components of Eq. (1) has been calculated from first principles as accurately as feasible, and more importantly at a level for which the remaining errors are expected to be insignificant. The resulting estimates for the rate constant, and particularly its energy dependence for low values of J, are then directly compared with corresponding state-of-the-art experimental measurements.

The singlet dissociation of ketene ($CH_2CO \rightarrow {}^1CH_2 + CO$) is chosen for this assessment for two reasons: (i) the availability of detailed, accurate, and wide-ranging experimental results,[5–14] and (ii) the feasibility of obtaining accurate quantum chemical predictions for the energetics of the transition state region. The relatively small size of ketene allows for the implementation of large basis sets and high levels of configuration interaction in the quantum chemical evaluations of the $CH_2 \cdots CO$ interaction energies. The near single-reference nature of the wave function along the singlet dissociation path further facilitates the accurate determination of electron correlation effects.

The photodissociation of ketene itself is quite complicated due to the presence of both singlet and triplet dissociation channels separated by only 1820 cm^{-1}. However, a wide variety of experimental[5–18] and theoretical studies[19–24] have led to this fragmentation being one of the best characterized dissociation processes. The initial photoexcitation occurs to vibrationally excited S_1 states ($\tilde{A}^1A''$) which may then relax via either intersystem crossing to T_1 ($\tilde{a}^{\,3}A''$) or via internal conversion back to the ground singlet state, S_0. A variety of observations suggest that these vibronic relaxation processes are rapid on the time scale of the dissociation. For photon energies ranging from the triplet threshold[15] of 28 296 cm^{-1} to the singlet threshold[6] of 30 116 cm^{-1}, dissociation must of course occur only on the lower-lying triplet state, which contains a small reverse barrier of 3.8 kcal/mol.[15] The wide-ranging photofragment excitation (PHOFEX) data of Moore and co-workers for the dynamics on this triplet state have been interpreted as evidence of quantized transition-state vibrational thresholds, which is a fundamental premise of RRKM theory.[15–18]

At higher excess energies the singlet and triplet dissociation channels are in direct competition, with the contribution of the triplet channel rapidly diminishing[7] as the excess energy increases due to the presence of the barrier along its dissociation path. Potter *et al.*[12] have performed time-resolved experimental measurements of the total dissociation rate constant for energies ranging from 450 to 5600 cm^{-1} in excess of the singlet threshold. The combination of these total dissociation rate constants with the measurements of Moore *et al.* of the singlet/triplet branching ratios[7] for energies ranging from the singlet threshold on up to 2500 cm^{-1} excess then directly provides the individual S_0 and T_1 dissociation rate constants. In each of these experiments, the rotational angular momentum was greatly restricted through a preliminary cooling of the reactants to about 3–4 K.

Moore and co-workers have also employed their PHOFEX technique as a means of probing the product rovibrational distributions for both the ${}^1CH_2$ and CO products.[5–11] These measurements have provided important indications of the limits of validity of various statistical theories such as phase space theory (PST),[25] which is an important limiting model. In particular, PST, which focuses on the energetics of the products, was found to provide very accurate descriptions of the rotational PHOFEX spectra,[5–7] particularly for lower excess energies. Meanwhile, PST is clearly in error for its predictions of the product vibrational distributions.[8,10,11] Interestingly, variational RRKM calculations[22,23] employing a model potential energy surface and certain assumptions for the dynamical motion from the transition state onwards[26] were able to simultaneously describe the earliest rovibrational distributions and the dissociation rate constants. However, the most recent observation of deviations of the rotational distributions from PST at energies below the threshold for vibrational excitation cannot be interpreted within this model.[10,11]

For concreteness this article will focus solely on the dissociation rate constants. However, the present quantum chemical data could also be used in calculations of the product state distributions, as was done in Ref. 23 using a simple model potential energy surface. An earlier first principles study[24] of the dissociation rate constants employed energetic estimates from second-order Møller–Plesset (MP2) perturbation theory with a 6-31G* basis set. The present study builds upon this preliminary work via the determination and implementation of substantially more accurate predictions for the interaction energies. In particular, the reaction path energies and force fields in the transition-state region are evaluated with state-of-the-art coupled-cluster techniques employing multiply polarized basis sets of quadruple-ζ quality, as described in Sec. II. These coupled-cluster interaction energies are also supplemented by corrections for basis set incompleteness and higher-order electron correlation effects. The results for the calculated reaction path energetics and force fields are summarized in Sec. III. The focus of these reaction path calculations is on an assumed bond-length reaction coordinate. However, the corresponding reaction path for a reaction coordinate defined by the separation between the fragment centers of mass is also obtained via analyses employing the bond-length reaction path force fields.

The present direct determination of the effect of anharmonicities on the transition-state number of states at the MP2/6-31G* level, as described in Sec. IV, provides a further improvement upon the preliminary study, which instead employed fitted analytic surfaces. Within this direct treatment explicit consideration is given to both bond-length and center-of-mass separation reaction coordinates. Next, the determination of the density of reactant states from a companion study of the anharmonic force field of ketene[27] is described in Sec. V. Finally, the resulting estimates for the rate constant are presented and compared to the corresponding experimental measurements in Sec. VI, with some concluding remarks made in Sec. VII. A preliminary communication of many aspects of this work has already appeared.[28]

II. QUANTUM CHEMICAL METHODS

Electronic energies on the singlet ketene surface were determined in this investigation by several electron correlation procedures, including Møller–Plesset perturbation theory through fourth order [MP2, MP3, and MP4(SDTQ)],[29–34] coupled-cluster techniques incorporating single and double substitutions (CCSD)[35–40] as well as a perturbative contribution from connected triple excitations [CCSD(T)],[41,42] and the Brueckner doubles (BD) method[43] with analogous corrections for both triple and quadruple excitations [BD(TQ)].[44–45] All reference electronic wave functions were constructed from single-configuration, restricted Hartree–Fock (RHF)[29,30,46] molecular orbitals. The carbon and oxygen $1s$ core orbitals were excluded from the active space in all correlation treatments together with the high-lying, core-localized virtual orbitals appearing above selected energy thresholds.[47] Final energetic predictions for the dissociation curve were derived from focal-point extrapolations[48,49] of the dual one-particle basis and higher-order correlation dependence of the $CH_2\cdots CO$ interaction energies. The total energies for the focal point analysis at each level of theory are given in the supplementary material at the end of this article (Table XII). The electronic structure computations were performed with the program packages PSI and GAUSSIAN92.[50,51]

The atomic-orbital basis sets employed here are denoted as 6-31G*, QZ($2d$,$2p$), QZ($2d1f$,$2p1d$), and [$13s8p6d4f$,$8s6p4d$] and consist of 49, 101, 132, and 377 contracted Gaussian functions, respectively. The 6-31G* basis set is the standard split-valence set of Pople and co-workers,[30,52] singly polarized for heavy atoms. The QZ(x,y) sets are nominally of quadruple-ζ quality, with x and y signifying the number and types of polarization manifolds centered on the (C,O) atoms and H atoms, in order. For carbon and oxygen, the QZ sp basis is comprised of the ($10s6p$) Gaussian primitives of Huzinaga[53] contracted to ($5s4p$) according to Dunning,[54] while for hydrogen an unscaled Huzinaga ($6s/4s$) contraction is used,[53] as tabulated by Allen and Schaefer.[55] The orbital exponents of the polarization functions augmenting the QZ sp sets are correlation-optimized values,[56] viz., α_d(C)=(0.318,1.097), α_f(C)=0.761, α_d(O)=(0.645, 2.314), α_f(O)=1.428, α_p(H)=(0.388, 1.407), and α_d(H)=1.057. The [$13s8p6d4f$,$8s6p4d$] basis is built up from the sp primitives of van Duijneveldt[57] and polarized with a collection of higher-l manifolds whose exponents are members of geometric series, with ratios of 0.4, fully spanning the space critical to the recovery of valence-shell correlation energy. The first exponents in these series are α_d(C)=7.12, α_f(C)=3.42, α_d(O)=12.65, α_f(O)=6.07, α_p(H)=9.88, and α_d(H)=4.0. In actuality, the [$13s8p6d4f$,$8s6p4d$] basis results by fully uncontracting the corresponding atomic-natural-orbital (ANO) sets of Almlöf and Taylor[58] and deleting the g and f manifolds for the (C,O) and H atoms, respectively. Except in the 6-31G* case, the supernumerary combinations of Cartesian d- and f-type polarization functions were excluded from the basis sets.

TABLE I. Equilibrium dipole moments (D) of ketene and singlet fragmentation products.

	CCSD/QZ($2d$,$2p$)[a]	CCSD(T)/QZ($2d1f$,$2p1d$)[a]	Expt.
CH_2CO ($\tilde{X}^1A_1$)	1.339	1.339	1.414[b]
CH_2 ($\tilde{a}^1A_1$)	1.763	1.752	⋯
CO ($\tilde{X}^1\Sigma^+$)	0.081	0.114	0.122[c]

[a]Evaluated as energy derivatives with respect to an external electric field.
[b]μ_0 from Ref. 60.
[c]μ_e from Ref. 61; μ_0=0.10980(3) D.

Two notable indicators attest to the reliability of the levels of theory implemented in this study. First, the Euclidean norm of the t_1 amplitudes of the CCSD/QZ($2d$,$2p$) wave function varies monotonically in the range $0.0197 \geqslant \|t_1\| \geqslant 0.0161$ for singlet $CH_2\cdots CO$ optimum structures with 2.2 Å$\leqslant R_{CC} \leqslant$3.1 Å, the $\|t_1\|$ values for CH_2CO, CO, and $^1CH_2$ being 0.0169, 0.0188, and 0.0093, respectively. Therefore, not only is a recommended standard[59] ($\|t_1\|<0.02$) consistently met for the degree of nondynamical correlation which can be readily accommodated by a single-reference wave function, but also the multireference character in the inner transition-state region of the fragmenting $CH_2\cdots CO$ system hardly exceeds that for the reactant and products. Second, the equilibrium dipole moments given in Table I for CH_2CO, CO, and $^1CH_2$ suggest that the CCSD/QZ($2d$,$2p$) and CCSD(T)/QZ($2d1f$,$2p1d$) levels of theory provide an excellent reproduction of the true charge distributions on the $CH_2\cdots CO$ surface.[60,61] In particular, the dipole moment of carbon monoxide, a widely chronicled *ab initio* benchmark,[62] is predicted within 0.01 D by the CCSD(T)/QZ($2d1f$,$2p1d$) method. Such agreement is requisite for proper convergence of the computed $CH_2\cdots CO$ interaction energies to the classical electrostatic limit at large distances.

Structures along the reaction path for singlet ketene fragmentation [R_{CC}(Å)=eq, 2.2, 2.5, 2.8, 3.1, and ∞] were optimized to 10^{-4} Å or rad at the CCSD/QZ($2d$,$2p$) and CCSD(T)/QZ($2d1f$,$2p1d$) levels of theory with the aid of analytic gradient techniques.[40,63] More extensive preliminary explorations of the reaction path for 1.46 Å$\leqslant R_{CC} \leqslant$3.1 Å were carried out in the same manner via MP2/6-31G* constrained optimizations. All CCSD(T)/QZ($2d1f$,$2p1d$) optimum structures were employed as reference geometries in the evaluation of complete CCSD/QZ($2d$,$2p$) quadratic force fields by means of finite differences of analytic gradients, using internal coordinate displacements of $\pm$0.005 Å and $\pm$0.01 rad. The efficacy of such CCSD/QZ($2d$,$2p$)// CCSD(T)/QZ($2d1f$,$2p1d$) force constant evaluations[64] is demonstrated by direct comparison of the resulting harmonic frequencies for CO and CH_2CO with their empirical counterparts. For carbon monoxide the predicted ω_e is only 3 cm^{-1} lower than experiment (2170 cm^{-1}),[61] whereas the average absolute error for the nine normal vibrations of ketene is a mere 1.06%.[27]

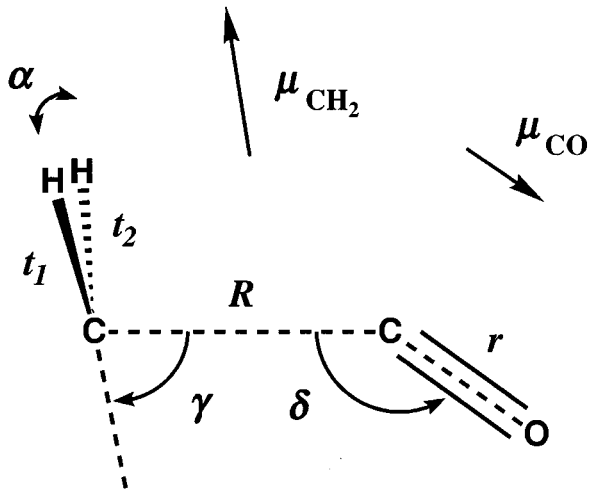

FIG. 1. A structural diagram depicting the internal coordinates of $CH_2\cdots CO$ employed in the reaction path fitting.

III. MAP OF THE REACTION PATH

A. Molecular structure

The fragmentation paths of the low-lying electronic states of ketene exhibit classic manifestations of the conservation of orbital symmetry.[65,66] On the S_0 surface, both least-motion (C_{2v}) and in-plane bent (C_s^{II}) dissociation paths are forbidden, whereas out-of-plane bent (C_s^{I}) distortions allow fragmentation without change of electronic configuration.[19,21] Indeed, explicit *ab initio* structural optimizations of the singlet $CH_2\cdots CO$ system in the inner transition-state region consistently yield out-of-plane, *trans*-bent conformations of the type depicted in Fig. 1. Optimum internal coordinates along the reaction path are given in Table II at the CCSD(T)/QZ($2d1f$,$2p1d$) and CCSD/QZ($2d$,$2p$) levels of theory along with analogous, earlier MP2/6-31G* predictions, and empirical data for the r_e structures of the reactant and products.

The theoretical bond distances in Table II exhibit a remarkable degree of relative uniformity; in particular, the differences between corresponding CCSD(T)/QZ($2d1f$,$2p1d$) and CCSD/QZ($2d$,$2p$) predictions for r_{CO} and t_{CH} lie in the narrow ranges [+0.0061,+0.0070] Å and [+0.0016, +0.0025] Å, respectively. The CCSD/QZ($2d$,$2p$) values for the same bonds in $^1CH_2$ and CH_2CO are within 0.001 Å of experiment, revealing that this intermediate level of theory happens to provide an exceedingly good balance of the key factors governing optimum bond distances for such chemical systems, i.e., contraction upon basis-set enlargement and elongation due to electron correlation.[69] In addition, the uniformity of bond-length shifts with level of theory and the comparison with end-point experimental structures suggests that essentially exact r_{CO} and t_{CH} predictions along the fragmentation path would be provided by constant −0.0057 and −0.0024 Å corrections, in order, to the CCSD(T)/QZ($2d1f$,$2p1d$) results.

For the methylene bond angle, the residual errors in the theoretical predictions for the dissociation path are less amenable to systematization. To wit, the CCSD(T)/QZ($2d1f$,$2p1d$) and CCSD/QZ($2d$,$2p$) α_{HCH} values reverse order and the CCSD(T)/QZ($2d1f$,$2p1d$) discrepancy vis-à-vis experiment changes sign in going from reactant to products. Nevertheless, the end-point calibrations suggest that the CCSD(T)/QZ($2d1f$,$2p1d$) angles deviate from those on the true path by no more than a few tenths of a degree. A reversal of order in the CCSD(T)/QZ($2d1f$,$2p1d$) and CCSD/QZ($2d$,$2p$) predictions is also observed for both the C–C–O bending (δ) and the CH_2 out-of-plane wagging (γ) angles, but the average separation among analogous δ and γ values is only 0.30° and 0.24°, respectively. It is notable that the MP2/6-31G* δ and γ predictions consistently

TABLE II. Optimum geometric coordinates along the fragmentation path of singlet ketene.[a,b]

	R_{CC}					
	eq[c]	2.2	2.5	2.8	3.1	∞
r_{CO}	1.1658(1.1597) **1.1603**[1.180]	1.1324(1.1254) [1.148]	1.1322(1.1256) [1.148]	1.1327(1.1262) [1.148]	1.1332(1.1267) [1.149]	1.1342(1.1278) **1.1283**[1.150]
t_{CH}	1.0782(1.0758) **1.0758**[1.081]	1.1089(1.1064) [1.108]	1.1101(1.1079) [1.108]	1.1101(1.1082) [1.108]	1.1101(1.1083) [1.108]	1.1103(1.1087) **1.108**[1.109]
α_{HCH}	121.88(121.98) **121.78**[120.8]	103.04(102.89) [103.1]	101.94(101.86) [102.2]	101.71(101.61) [102.0]	101.68(101.55) [102.0]	101.76(101.60) **102.1**[102.1]
δ_{CCO}	180	159.50(160.18) [156.6]	162.15(162.42) [159.6]	163.85(163.83) [159.6]	164.55(164.30) [163.2]	180
γ_{CH_2}	0	−89.23(−89.45) [−87.63]	−94.67(−94.60) [−92.59]	−98.09(−97.85) [−94.89]	−100.49(−100.07) [−97.38]	−180

[a]Bond lengths in Å, bond angles in degrees (°). Negative values of γ imply *trans* configurations. See Fig. 1 for a structural depiction.

[b]The principal entries are CCSD(T)/QZ($2d1f$,$2p1d$) values, whereas the data in parentheses and brackets are CCSD/QZ($2d$,$2p$) and MP2/6-31G* results, respectively. The MP2/6-31G* parameters are taken from Ref. 24 and may only be converged to a few thousandths of an Å or a few tenths of a degree. Experimental equilibrium parameters for the ketene reactant (Ref. 27) and the methylene (Ref. 67) and carbon monoxide (Ref. 68) products are also listed in boldface type.

[c]Equilibrium carbon–carbon distance for each method; R_e(C–C) (Å) = 1.3189 [CCSD(T)/QZ($2d1f$,$2p1d$)], 1.3155 [CCSD/QZ($2d$,$2p$)], 1.318 [MP2/6-31G*], and 1.3121 [expt., Ref. 27].

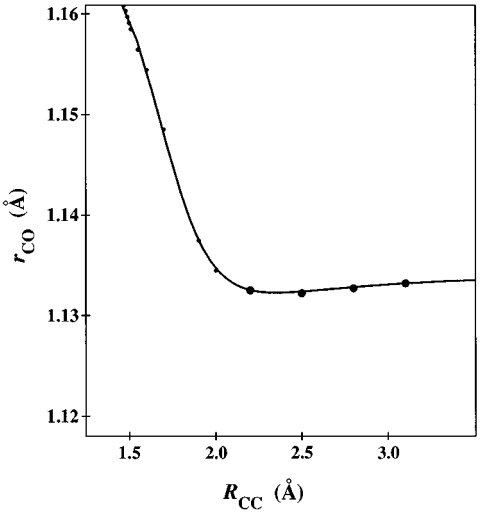

FIG. 2. Plot of the optimum C–O bond length along the ketene fragmentation path as defined by the C–C bond-length reaction coordinate. The filled circles denote the *ab initio* data, while the solid line denotes the fit to this data given in Table III.

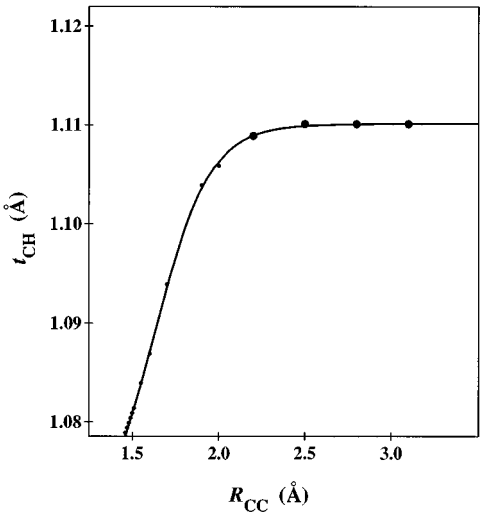

FIG. 3. The optimum C–H bond length along the reaction path, à la Fig. 2.

lag their coupled-cluster counterparts by 1.1–4.3°.

In order to probe the reaction path outside the inner transition-state region, the evolution of the singlet $CH_2\cdots CO$ structure was followed at the MP2/6-31G* level for a range of smaller R_{CC} distances, including 2.0, 1.9, 1.7, 1.6 Å, and a cluster of separations between 1.55 and 1.46 Å. A global map was then constructed by splicing the resulting points to the more reliable CCSD(T)/QZ($2d1f$,$2p1d$) curves, specifically, adding to the optimum MP2/6-31G* coordinates at each interfragment distance a constant shift selected to knot the two data sets at $R_{CC}=2.2$ Å. Because the region inside 2.2 Å is fully contained by the ensemble of transition-state dividing surfaces for singlet dissociation (at least for the energies of interest here), any inaccuracies arising from the splicing technique have no bearing on the statistical treatment of the kinetics. The conjoined CCSD(T)/QZ($2d1f$,$2p1d$) and MP2/6-31G* results for the internal coordinate variations along the reaction path are plotted in Figs. 2–6, wherein the primary CCSD(T)/QZ($2d1f$,$2p1d$) points are enlarged. The spliced data sets clearly exhibit high internal consistency, except perhaps in the case of δ_{CCO}.

The bifurcation point marking the advent of the C_s^I dissociation path, where ketene first distorts from C_{2v} symmetry out of the molecular plane, occurs in the vicinity of $R_{CC}=1.46$ Å,[70] only about 0.15 Å past the equilibrium position on the surface. Relative to the r_e structure of ketene, the bifurcation point displays slightly contracted (0.003 Å) C–O and C–H bonds, and a methylene bond angle which is actually widened by 4°. As *trans*-bending deformation progresses prior to reaching the inner transition state threshold (2.2 Å), the C–O bond contracts further by 0.03 Å, the C–H distance elongates by 0.03 Å, the α_{HCH} angle shrinks by 22°, and the methylene framework wags out of plane by 90°. The concomitant variations of δ_{CCO} are more peculiar—a minimum near 158° is traversed just before the transition-state threshold is reached.

The trajectory of the reaction path through the transition-state region and onward to products has important implications for the dissociation dynamics. In particular, the structures of the carbon monoxide and methylene fragments are essentially static for $R_{CC}\geqslant 2.2$ Å. The bond lengths have approached their respective asymptotic limits within 0.002 Å by $R_{CC}=2.2$ Å, and after 2.5 Å the α_{HCH} angle varies less than 0.3°. The constancy of these optimum coordinates throughout the transition-state region indicates a nearly complete decoupling of the associated vibrational modes from complementary motions along the reaction path.

In contrast to the intrafragment variables, the orientational coordinates δ and γ exhibit an extremely slow decay

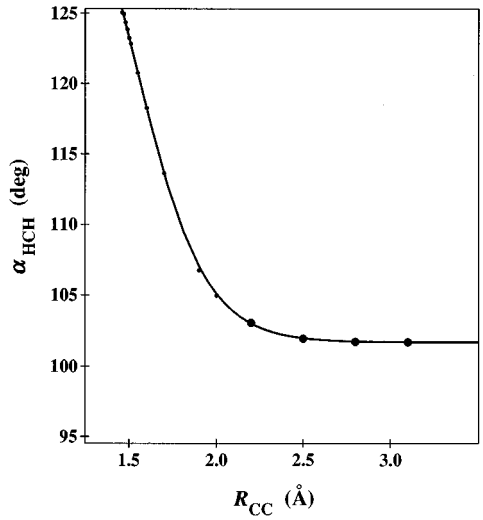

FIG. 4. The optimum H–C–H bending angle along the reaction path, à la Fig. 2.

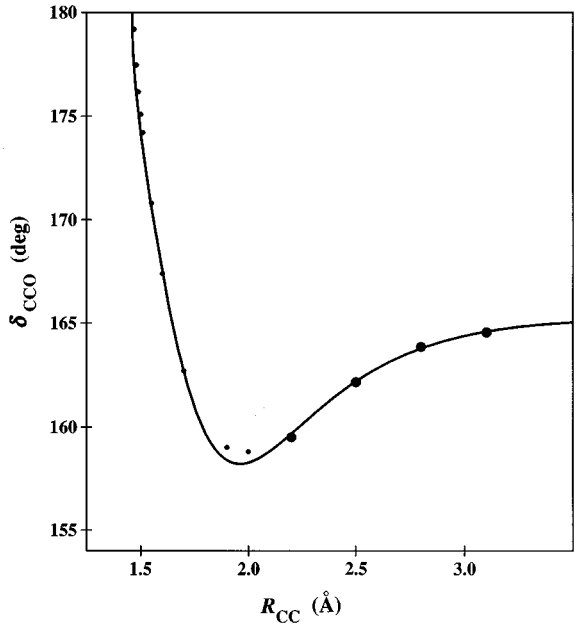

FIG. 5. The optimum C–C–O bending angle along the reaction path, à la Fig. 2.

TABLE III. Analytic parametrizations for the fragmentation path of singlet ketene.[a,b]

$$r_{CO}(R) = 1.1343 - \frac{0.033}{R^3} + 0.023\,732\,2\{1 - \tanh[3.260\,46(R - 1.656\,84)]\}$$

$$t_{CH}(R) = 1.1103 - \frac{0.000\,56}{R} - 0.021\,269\,9\{1 - \tanh[3.14376(R - 1.62417)]\}$$

$$\alpha_{HCH}(R) = 101.76 - \frac{0.248}{R} + 20.465\{1 - \tanh[2.50275(R - 1.52386)]\}$$

$$\delta_{CCO}(R) = 180[1 - f_\delta(R)\sqrt{R - 1.46}]$$

$$f_\delta(R) = 1.372\,24(R+5)^{-3/2} + 11.1345\exp[-2.363\,77R] - 0.749\,945 \times \exp[-4.510\,56(R-1)^2]$$

$$\gamma_{CH_2}(R) = \frac{-180(R - 1.46)^{1/4}}{f_\gamma(R) + (R - 1.46)^{1/4}}$$

$$f_\gamma(R) = 0.893\,269 + 157.681\exp[-3.659\,78\ R] + \frac{2.095\,78}{[10(R - 1.359\,17)]^4}$$

[a]Distances in Å, angles in degrees (°). See Fig. 1 for a structural depiction and pictorial definitions of the internal coordinates. The parametric equations are plotted in Figs. 2–6.

[b]Replacement of the constants 1.1343 and 1.1103 for r_{CO} and t_{CH} by 1.1286 and 1.1079, in order, provides essentially exact reproduction of the empirical structures of the reactant and products, as explained in the text.

to their respective asymptotes of 180° and −180°. These limits seem enigmatic at first but are readily elucidated by considerations of long-range classical electrostatics. In Fig. 1 the dipole moment vectors for the free fragments are depicted in relation to the *trans*-bent transition-state structures. Because the partial negative charge in CO appears on the carbon atom, the methylene moiety must eventually flip to provide alignment of the dipole vectors. The arrows associated with δ and γ in Fig. 1 show the progression of this reorientation with continuing fragmentation. Notwithstanding dipole alignment effects, the dominant $CH_2\cdots CO$ interaction[71] for intermediate separations is the incipient bond formation among frontier orbitals, involving the donation of σ electron density from a carbonyl lone pair into the empty p orbital of the methylene carbon. This chemical bonding is maximized for nearly orthogonal conformations with γ close to −90° but destroyed by the full reorientation resulting at long range from classical electrostatics. Accordingly, the approach of δ and γ to their asymptotic limits is severely retarded.

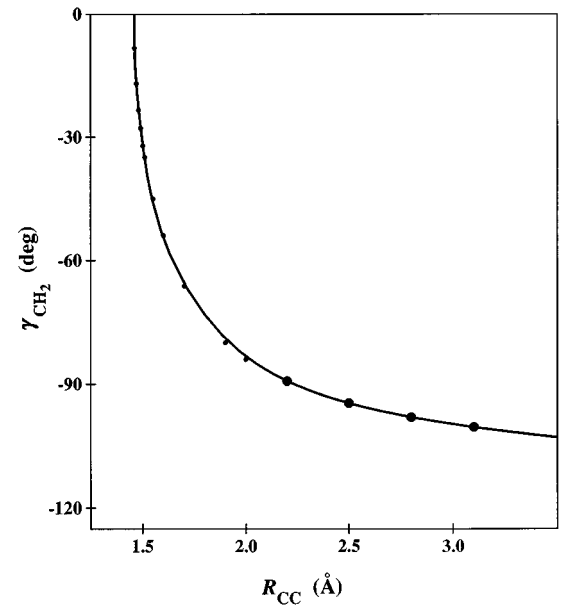

FIG. 6. The optimum out-of-plane angle γ along the reaction path, à la Fig. 2.

Analytic parametrizations of the optimum internal coordinate variations along the fragmentation path are given in Table III. These functional forms are not required for the present variational statistical treatment of the dissociation kinetics (Sec. IV) but should facilitate future developments of analytic potential energy surfaces for sundry purposes, including dynamical simulations. As shown in Figs. 2–6, the parametrizations provide an excellent fit of the conjoined CCSD(T)/QZ($2d1f$,$2p1d$) and MP2/6-31G* data, the only point of difficulty being the turnover region of δ_{CCO}, where the curvature of the MP2/6-31G* points themselves appears somewhat deficient. For very large interfragment separations, the present forms only give the proper asymptotes; explicit *ab initio* data for $R_{CC} \gg 3.1$ Å would be needed to ensure quantitative parametrizations. Moreover, a long-range bifurcation point which engenders kinks in the optimum coordinate dependences on R_{CC} has been ignored. Specifically, once the fragment separation exceeds a critical distance for effectual chemical bonding, dipole alignment forces return the system to C_{2v} optimum structures. Thus, the *trans*-bent C_s^I reaction path is actually anchored to the C_{2v} configuration space at both end points, beginning with strongly

TABLE IV. Focal-point analysis of the dissociation energy (D_e) of singlet ketene.[a]

	$CH_2(^1A_1)+CO \rightarrow CH_2CO(^1A_1)$			
	6-31G*	QZ(2*d*,2*p*)	QZ(2*d*1*f*,2*p*1*d*)	[13*s*8*p*6*d*4*f*,8*s*6*p*4*d*]
ΔE_e[RHF]	−25 125	−24 156	−24 630	−24 521
δ[MP2]	−9191	−9191	−9986	−10192
δ[MP3]	+2466	+2911	+2808	[+2808]
δ[CCSD] (δ[MP4])	+1544 (−192)	+1651 (−330)	+1648 (−449)	[+1648]
δ[CCSD(T)]	−732	−944	−1010	[−1010]
δ[BD(TQ)]	+107	{+137}	{+147}	{+147}
ΔE_e (corr)	−30 931	{−29 592}	{−31 023}	{−31 120}

$\Delta E_e[fp] = -31\,120$ cm^{-1} BAC $= -1126$ cm^{-1} Final value: $D_e = 32246$ cm^{-1}

[a]All entries in cm^{-1}; based on optimum QZ(2*d*1*f*,2*p*1*d*) CCSD(T) reference geometries. The symbol δ denotes the *increment* in the binding energy (ΔE_e) relative to the preceding level of theory in the correlation series RHF→MP2→MP3→CCSD (MP4)→CCSD(T)→BD(TQ). The {13*s*8*p*6*d*4*f*,8*s*6*p*4*d*} increments in brackets are assumed values taken from the corresponding QZ(2*d*1*f*,2*p*1*d*) predictions. The (Q) corrections appearing in braces for the effect of connected quadruple excitations with the larger basis sets were estimated from the explicit 6-31G* results via the following scaling formula: $\delta[\mathrm{BD(TQ)}]_x = \delta[\mathrm{BD(TQ)}]_{6\text{-}31G^*} (\delta[\mathrm{CCSD(T)}]_x / \delta[\mathrm{CCSD(T)}]_{6\text{-}31G^*})$, where x=QZ(2*d*,2*p*), QZ(2*d*1*f*,2*p*1*d*), and [13*s*8*p*6*d*4*f*,8*s*6*p*4*d*]. The final bond additivity corrections (BACs) were computed via Eq. (2).

bonded $(\delta,\gamma)=(180°,0°)$ structures for small separations and ending with loosely interacting $(\delta,\gamma)=(180°,-180°)$ complexes at large distances.

B. Energetics of dissociation

The potential energy curves for the cleavage of covalent chemical bonds embody large differential correlation effects between end points, whose full recovery requires rigorous, higher-order correlation treatments with large, multiply-polarized one-particle basis sets.[56,72] The attendant demand on resources can rarely be met. However, precise knowledge of the potential surface in the variational transition-state region is critical to any quantitative statistical analysis of a barrierless reaction such as singlet ketene fragmentation. The present study is particularly distinguished from earlier work on singlet ketene in its progressive pursuit of a quantitative dissociation curve, starting with explicit QZ(2*d*1*f*,2*p*1*d*) CCSD(T) reference predictions and continuing with systematic corrections for residual limitations. The foundation for estimating these corrections is a focal-point extrapolation[48] of both basis set dependence and higher-order correlation terms augmented by an empirically based bond-additivity correction (BAC). Several recent thermochemical studies[48,49] exemplify the original technique, which is extended here to directly include the effects of connected quadruple excitations and to account for the decay of the BAC with increasing interfragment separation.

The focal-point energetic analysis is calibrated in Table IV on the dissociation energy (D_e) of singlet ketene. For each basis set the total energy change for bond formation is partitioned as an initial ΔE_e[RHF] term followed by successive correlation *increments* (δ) for this quantity in the primary series RHF→MP2→MP3→CCSD→CCSD(T)→BD(TQ). Hence, the binding energy computed at a given level of theory is ascertained by summing the entries down the relevant basis-set column until the corresponding correlation technique is reached. The extent of the decay of the successive terms toward zero is a gauge of the reliability of the final electronic structure predictions. As observed repeatedly,[48,49] the focal-point construction isolates in large part the slow basis-set convergence of differential correlation effects in the second-order increment δ[MP2], exposing the more rapid absolute convergence of analogous higher-order terms and facilitating the dual extrapolation of the final energy change ($\Delta E_e[fp]$) toward the one- and n-particle limits. The changes in the binding energy increments upon the QZ(2*d*,2*p*)→QZ(2*d*1*f*,2*p*1*d*) augmentation exemplify this general behavior;[73] specifically, the shifts $\Delta(\delta[\mathrm{RHF}], \delta[\mathrm{MP2}]) = (474, 795)$ cm^{-1} substantially exceed their counterparts $\Delta(\delta[\mathrm{MP3}], \delta[\mathrm{CCSD}], \delta[\mathrm{CCSD(T)}]) = (103, 3, 66)$ cm^{-1}. Indeed, convergence of higher-order increments even to 0.1 kcal mol^{-1} for basis sets of this type does not appear uncommon.[48,49] In accord with such observations, the higher-order correlation terms for the [13*s*8*p*6*d*4*f*,8*s*6*p*4*d*] basis are taken from corresponding QZ(2*d*1*f*,2*p*1*d*) predictions in the fp extrapolation procedure, as signified by the brackets in Table IV. The connected quadruples (Q) correction for the dissociation energy, whose evaluation is feasible only with the 6-31G* basis, is −0.31 kcal mol^{-1}. Because the antecedent 6-31G* triples (T) increment increases by 30–40 % upon basis-set augmentation, the corresponding δ[BD(TQ)] term is deemed too small in magnitude by roughly 0.1 kcal mol^{-1}. In Table IV, an adjustment reckoned by the simple scaling formula given in footnote *a* provides the compensated entries listed in braces.

A precise experimental threshold for the singlet dissociation channel[6] of ketene and definitive anharmonic force fields of CH_2CO,[27] singlet methylene,[74] and carbon monoxide[68] yield an accurate empirical value of 32 246 cm^{-1} for the vibrationless dissociation energy (D_e). Despite the extensive computations of the present focal-point analy-

sis, the resulting binding energy ($-\Delta E_e[fp]=31\ 120\ \mathrm{cm}^{-1}$) is thus 1126 cm^{-1} too small, primarily due to the incompleteness of the angular momentum space even in the largest basis sets employed here.[56,72,75] Accordingly, a reasonable bond additivity correction (BAC) function to account for the residual errors in $-\Delta E_e[fp]$ along the reaction path is simply $\mathrm{BAC}(R_{\mathrm{CC}})=1126\ f(R_{\mathrm{CC}})\ \mathrm{cm}^{-1}$, where the scaling fraction is given by

$$f(R_{\mathrm{CC}})=\frac{\{\Delta E_e[R_{\mathrm{CC}};\mathrm{CCSD(T)/QZ}(2d1f,2p1d)]-\Delta E_e[R_{\mathrm{CC}};\mathrm{CCSD(T)/QZ}(2d,2p)]\}}{\{\Delta E_e[R_e;\mathrm{CCSD(T)/QZ}(2d1f,2p1d)]-\Delta E_e[R_e;\mathrm{CCSD(T)/QZ}(2d,2p)]\}}. \tag{2}$$

With this expression $f(R_{\mathrm{CC}})$ takes on the values 0.1382, 0.05025, 0.01464, and 0.00090 at $R_{\mathrm{CC}}=2.2$, 2.5, 2.8, and 3.1 Å, respectively. The rapid decay of $f(R_{\mathrm{CC}})$ is indeed consistent with the expected exponential falloff of the fragment wave function overlap and in line with exponential forms of BAC factors employed in established, predictive thermochemical methodologies.[76]

The focal-point analyses for the transition-state energetics along the dissociation path of singlet ketene are displayed in Table V. The binding energy in this critical region varies from 13.8 kcal mol^{-1} at $R_{\mathrm{CC}}=2.2$ Å down to 2.5 kcal mol^{-1} at $R_{\mathrm{CC}}=3.1$ Å, as compared to $D_e=92.2$ kcal mol^{-1}. The corresponding BAC corrections range from 0.44 to less than 0.01 kcal mol^{-1}, whereas the compensated (Q) terms go from -0.16 to -0.05 kcal mol^{-1}, comprising 10–20 % of the analogous (T) contributions. The refinement of the reaction path potential from the earliest model function[22] to the current focal-point+BAC curve is illustrated in Fig. 7. The simple model potential is seen to seriously underestimate the interaction energies, illustrating the difficulty of treating the reaction dynamics without reliable *ab initio* input. However, both the MP2/6-31G* and the CCSD/QZ($2d$,$2p$) methods seem to predict the binding energy curve to better than 20% in the transition-state region, apparently bracketing the true potential. Finally, the propinquity of the CCSD(T)/QZ($2d1f$,$2p1d$) and final focal-point+BAC curves is both striking and comforting, the deviation of the former relative to the latter varying from -2.5 to $+4.2$% over the transition-state region.

C. Quadratic force fields

The orientational dependence of interfragment interactions and the associated coupling to both intrafragment modes and the reaction coordinate is paramount to the dissociation kinetics of the singlet $\mathrm{CH_2}\cdots\mathrm{CO}$ system. The quadratic force field along the reaction path, the primary indicator of such interactions, was thus evaluated via the CCSD/QZ($2d$,$2p$)//CCSD(T)/QZ($2d1f$,$2p1d$) approach for R_{CC}(Å)=2.2, 2.5, 2.8, 3.1, and ∞. As mentioned above, calibrations for the reactant and product suggest a mean accuracy of about 1% for the harmonic frequencies arising from these force fields, obviating the need for any scaling of the elements. The force constants F_{ij} are collected in Table VI, which also includes a definition of the C_s^I symmetry internal coordinates adopted for the evaluation and representation of the quadratic vibrational field. The numbering of the variables is chosen for direct correspondence with the spectroscopic ordering of the normal modes of the ketene reactant.[27] Because the bonding environment about the methylene carbon is highly pyramidal throughout the inner transition-state region (*n.b.*, Fig. 1), the symmetric combination of H–C–C angles [$S_6(a')$] provides an effective nonsingular alternative to the out-of-plane wagging coordinate (γ). The convenience of this substitution is that the antisymmetric analog [$S_8(a'')$] describes the methylene rocking mode, which for nearly orthogonal interfragment conformations is best viewed as a twisting motion about the local $\mathrm{CH_2}$ symmetry axis. The torsional coordinate [$S_9(a'')$] complementary to such twisting involves internal rotation of the $\mathrm{CH_2}$ and CO fragments about the C–C axis. The methylene excursions entailed by the S_6, S_8, and S_9 variables correlate, respectively, to b-, a-, and c-axis rotations of $\mathrm{CH_2}$ at infinite separation.

The physics of the dissociation process which provides the basis for the current implementation of variational RRKM methods is described naturally by the chosen C_s^I coordinate set. First, the reaction coordinate (R_{CC}) is precisely $S_4(a')$ alone. Next, the $S_1(a')$, $S_2(a')$, $S_3(a')$, and $S_7(a'')$ coordinates are in one-to-one correspondence with the internal vibrations of $^1\mathrm{CH_2}$ and CO, which are static in character during the dissociation, particularly in the critical stages, and are termed conserved modes. Finally, the orientational motions represented by $S_5(a')$, $S_6(a')$, $S_8(a'')$, and $S_9(a'')$ transform from vibrations to free rotations during the dissociation process and are thus termed transitional modes. The partitioning of the molecular degrees of freedom into conserved and transitional modes complementary to the reaction coordinate is central to the formalism of the statistical analysis performed here. The quadratic force constants in Table VI are blocked accordingly.

The nonvanishing force constants for the conserved modes have approached their asymptotic limits within 2% even at the inner transition-state threshold (2.2 Å), except for F_{33}, which relaxes to this level by 2.5 Å, in accord with the underlying variations in α_{HCH} (*vide supra*). As expected, the force constants in the transitional-mode space exhibit an approximately exponential approach to zero, with a characteristic decay constant between 1.5 and 3.0 $\mathrm{Å}^{-1}$ vis-à-vis the reaction coordinate. It is notable that the MP2/6-31G* force constants computed previously[24] for the transitional modes, and listed as secondary entries in Table VI, lie within 10% of their CCSD/QZ($2d$,$2p$)//CCSD(T)/QZ($2d1f$,$2p1d$) coun-

TABLE V. Focal-point analyses of the binding energy (ΔE_e) at intermediate distances along the dissociation path of singlet ketene.[a]

	6-31G*	QZ(2d,2p)	QZ(2d1f,2p1d)	[13s8p6d4f,8s6p4d]
	$CH_2(^1A_1)+CO \rightarrow CH_2\cdots CO(^1A', R_{CO}=2.2$ Å)			
ΔE_e[RHF]	−2164	−1735	−1801	−1711
δ[MP2]	−2617	−3335	−3463	−3579
δ[MP3]	+666	+770	+772	[+772]
δ[CCSD] (δ[MP4])	+300(−445)	+402(−534)	+423(−557)	[+423]
δ[CCSD(T)]	−425	−598	−626	[−626]
δ[BD(TQ)]	+38	{+54}	{+57}	{+57}
ΔE_e(corr)	−4201	{−4442}	{−4638}	{−4664}
$\Delta E_e[fp]=-4664$ cm^{-1}	BAC=−154 cm^{-1}		Final value: ΔE_e (2.2 Å)=−4818 cm^{-1}	
	$CH_2(^1A_1)+CO \rightarrow CH_2\cdots CO$ ($^1A'$, $R_{CC}=2.5$ Å)			
ΔE_e[RHF]	−1380	−996	−1026	−948
δ[MP2]	−1279	−1713	−1758	−1838
δ[MP3]	+315	+354	+356	[+356]
δ[CCSD] (δ[MP4])	+219(−210)	+267(−252)	+281(−259)	[+281]
δ[CCSD(T)]	−174	−276	−289	[−289]
δ[BD(TQ)]	+24	{+38}	{+40}	{+40}
ΔE_e(corr)	−2275	{−2325}	{−2396}	{−2398}
$\Delta E_e[fp]=-2398$ cm^{-1}	BAC=−56 cm^{-1}		Final value: ΔE_e (2.5 Å)=−2454 cm^{-1}	
	$CH_2(^1A_1)+CO \rightarrow CH_2\cdots CO$ ($^1A'$, $R_{CC}=2.8$ Å)			
ΔE_e[RHF]	−965	−682	−697	−630
δ[MP2]	−684	−921	−930	−987
δ[MP3]	+167	+181	+182	[+182]
δ[CCSD](δ[MP4])	+123(−116)	+149(−136)	+157(−137)	[+157]
δ[CCSD(T)]	−79	−135	−141	[−141]
δ[BD(TQ)]	+14	{+25}	{+26}	{+26}
ΔE_e(corr)	−1424	{−1383}	{−1403}	{−1393}
$\Delta E_e[fp]=-1393$ cm^{-1}	BAC=−16 cm^{-1}		Final value: ΔE_e (2.8 Å)=−1409 cm^{-1}	
	$CH_2(^1A_1)+CO \rightarrow CH_2\cdots CO$ ($^1A'$, $R_{CC}=3.1$ Å)			
ΔE_e[RHF]	−655	−483	−491	−435
δ[MP2]	−388	−524	−520	−557
δ[MP3]	+99	+106	+106	[+106]
δ[CCSD] (δ[MP4])	+66(−69)	+78(−83)	+82(−82)	[+82]
δ[CCSD(T)]	−39	−72	−74	[−74]
δ[BD(TQ)]	+9	{+16}	{+17}	{+17}
ΔE_e(corr)	−908	{−878}	{−879}	{−860}
$\Delta E_e[fp]=-860$ cm^{-1}	BAC=−1 cm^{-1}		Final value: ΔE_e (3.1 Å)=−861 cm^{-1}	

[a]All entries in cm^{-1}; based on optimum QZ(2d1f,2p1d) CCSD(T) reference geometries for each R_{CC} distance. See also footnote a of Table IV.

terparts for each intermediate structure in every case but the diagonal $CH_2\cdots CO$ torsion element F_{99}, which is apparently underestimated by a factor near 1.5 at the MP2/6-31G* level. The extent of this overall agreement firmly validates the use of MP2/6-31G* computations to incorporate orientational-mode anharmonicity in the direct statistical enumeration of the accessible states in the transition-state region. Of the interaction constants coupling the conserved, transitional, and reaction coordinate spaces, several exhibit intricacies in their decay toward zero, such as the sign changes occurring for F_{42} and F_{61} or the nonmonotonicity of F_{87}. However, the weakness of the couplings, as manifested in the diagonal dominance of the F_{ij} matrix, renders these variations insignificant to the dissociation process.

The harmonic frequencies given by the CCSD/QZ(2d,2p)//CCSD(T)/QZ(2d1f,2p1d) force fields for the orthogonal modes along the dissociation path are listed in Table VII and compared therein both to analogous MP2/6-31G* predictions and empirically based ω_i values for the reactant and product. The technique employed for the vibrational analyses[79] also allows the ascription of the frequencies appearing in Table VII for reaction coordinate motion, providing a measure of the negative curvature of the bonding potential at the various interfragment separations. Apart from the aforementioned 0.3 Å delay in the relaxation of the methylene bending mode, the intrafragment vibrational frequencies vary no more than 20 cm^{-1} past the inner transition-state threshold. The adiabaticity of the conserved

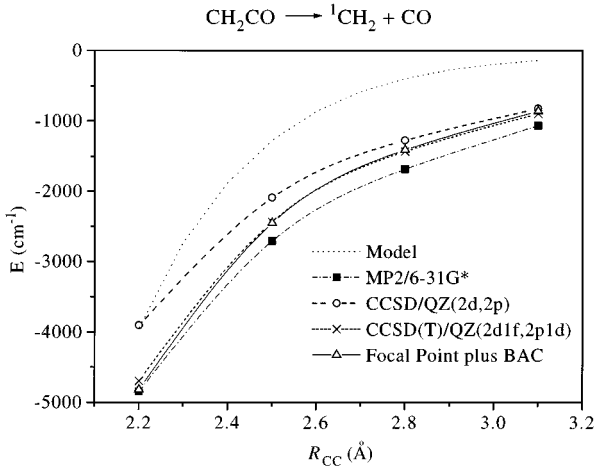

FIG. 7. Plot of the minimum potential energy along the reaction path as defined by the value of the C–C bond length. The dotted line denotes the model potential of Ref. 24, whereas the other curves are present results.

modes is even more vividly demonstrated by the constancy of the zero-point vibrational energy in this space, which is 4736, 4742, 4746, and 4746 cm^{-1} at R_{CC}(Å)=2.2, 2.5, 2.8, and 3.1, respectively. The in-plane (a') transitional modes of the R_{CC}=2.2 Å structure are of much different character than the antecedent b_1 normal vibrations of ketene, having transformed during the $C_{2v} \rightarrow C_s^I$ distortion from fully mixed *cis* and *trans* combinations of CH_2 wagging and C–C–O bending[27] to almost completely decoupled local vibrations, with a concomitant splitting of (ω_5,ω_6) from (590,507) to (971,187) cm^{-1}. The out-of-plane (a'') transitional modes are not so strongly coupled in the reactant and thus are merely loosened rather than split by the preliminary C_s^I distortion, whence the (ω_8,ω_9) pair changes from (1018,436) to (804,178) cm^{-1}. Notwithstanding the early, varied evolution of the interfragment modes, all transitional-mode frequencies diminish smoothly past R_{CC}=2.2 Å, in accord with the approximate exponential decay previously noted in the underlying force constants. The degree to which the MP2/6-31G*

TABLE VI. Symmetry internal coordinates (S_i) and quadratic force constants (F_{ij}) along the fragmentation path of singlet ketene.[a,b]

$S_1=2^{-1/2}(t_1+t_2)$ (sym. C–H stretch)	$S_4=R$ (C–C stretch)	$S_7=2^{-1/2}(t_1-t_2)$ (asym. C–H stretch)
$S_2=r$ (C–O stretch)	$S_5=\delta$ (C–C–O bend)	$S_8=2^{-1/2}(\beta_1-\beta_2)$ (CH_2 rock/twist)
$S_3=\alpha$ (CH_2 scissor)	$S_6=2^{-1/2}$ $(\beta_1+\beta_2)$ (CH_2 wag)	$S_9=2^{-1/2}(\tau_1+\tau_2)$ ($CH_2\cdots CO$ torsion)

ij	R_{CC} (Å)				
	2.2	2.5	2.8	3.1	∞
			Conserved modes		
11 (a')	4.7768	4.7435	4.7425	4.7432	4.7338
21	−0.0013	−0.0093	−0.0098	−0.0089	0
22	19.098	19.211	19.161	19.111	18.977
31	0.3175	0.3196	0.3181	0.3162	0.3124
32	−0.0309	−0.0078	−0.0026	−0.0011	0
33	0.6602	0.6907	0.6994	0.7014	0.6967
77 (a'')	4.8245	4.7880	4.7852	4.7843	4.7722
			Transitional modes		
55 (a')	0.1437(0.14)	0.0676(0.061)	0.0375(0.035)	0.0233(0.023)	0
65	0.1451(0.14)	0.0801(0.080)	0.0437(0.045)	0.0251(0.026)	0
66	0.5704(0.60)	0.3604(0.37)	0.2019(0.20)	0.1075(0.11)	0
88 (a'')	0.4324(0.44)	0.2345(0.24)	0.1113(0.11)	0.0499(0.051)	0
98	−0.0194(−0.019)	−0.0083(−0.0085)	−0.0036(−0.0034)	−0.0017(−0.0017)	0
99	0.0058(0.0078)	0.0024(0.0039)	0.0012(0.0019)	0.0007(0.0009)	0
			Conserved/transitional mode coupling		
51 (a')	−0.0095	−0.0126	−0.0093	−0.0062	0
52	0.0375	0.0048	−0.0038	−0.0052	0
53	−0.0218	−0.0132	−0.0086	−0.0058	0
61	0.0212	−0.0224	−0.0256	−0.0184	0
62	−0.0263	−0.0146	−0.0139	−0.0129	0
63	−0.0790	−0.0576	−0.0391	−0.0255	0
87 (a'')	−0.0282	−0.0443	−0.0340	−0.0211	0
97	0.0084	0.0050	0.0030	0.0019	0
			Reaction coordinate coupling		
41 (a')	−0.0220	−0.0083	−0.0048	−0.0033	0
42	0.0492	−0.0447	−0.0401	−0.0271	0
43	0.0444	0.0078	−0.0008	−0.0019	0
44	−0.5420	−0.1848	−0.0700	−0.0354	0
54	0.0315	0.0092	0.0042	0.0024	0
64	0.1668	0.0656	0.0269	0.0115	0

[a]See Fig. 1 for a structural depiction and pictorial definitions of the internal coordinates; β_i and τ_i denote the H_i–C–C bending and H_i–C–C–O dihedral angles, respectively.

[b]Force constant units consistent with energy in aJ, distances in Å, and angles in rad. The principal entries are CCSD/QZ(2*d*,2*p*)//CCSD(T)/QZ(2*d*1*f*,2*p*1*d*) values, and those in parentheses are MP2/6-31G* results.

TABLE VII. Harmonic frequencies (cm^{-1}) along the fragmentation path of singlet ketene.[a]

	R_{CC} (Å)					
	eq	2.2	2.5	2.8	3.1	∞
			Conserved modes			
$\omega_1(a_1,a')$ sym. C–H str.	[**3202**] 3194 (3263)	2919 (3007)	2912 (3002)	2912 (3006)	2912 (3006)	2908 (3002)
$\omega_2(a_1,a')$ C–O str.	[**2197**] 2170 (2243)	2166 (2139)	2178 (2141)	2177 (2138)	2175 (2132)	[**2170**] 2167 (2125)
$\omega_3(a_1,a')$ CH_2 scissor	[**1415**] 1442 (1454)	1393 (1475)	1414 (1492)	1423 (1499)	1426 (1500)	[**1401**][b] 1426 (1499)
$\omega_7(b_2,a'')$ asym. C–H str.	[**3308**] 3300 (3367)	2995 (3103)	2981 (3094)	2980 (3096)	2979 (3090)	2975 (3086)
			Transitional modes			
$\omega_5(b_1,a')$ CH_2 wag	[**582**] 590 (588)	971 (1001)	769 (791)	571 (581)	414 (415)	0
$\omega_6(b_1,a')$ C–C–O bend	[**503**] 507 (528)	187 (190)	125 (117)	92 (86)	71 (68)	0
$\omega_8(b_2,a'')$ CH_2 rock/twist	[**996**] 1018 (1022)	804 (812)	584 (589)	400 (401)	267 (272)	0
$\omega_9(b_2,a'')$ $CH_2\cdots CO$ torsion	[**434**] 436 (443)	178 (185)	127 (136)	96 (106)	76 (82)	0
			Reaction coordinate			
$\omega_4(a_1,a')$ C–C str.	[**1146**] 1156 (1176)	321*i*	186*i*	114*i*	81*i*	0

[a]The principle theoretical entries are CCSD/QZ (2*d*,2*p*)//CCSD(T)/QZ(2*d*1*f*,2*p*1*d*) values, and those in parentheses are MP2/6-31G* results. Empirically based harmonic frequencies are listed as boldface quantities in brackets for the reactant (ketene, Ref. 27) and products $^1CH_2$, Refs. 74, 77, and 78; CO, Ref. 68).
[b]Extracted via second-order perturbation theory from the experimental band origins collected in Table IV of Ref. 78.

frequencies in Table VII reproduce the higher level predictions for the decay of the transitional modes is striking, further documenting the use of this level of theory to probe interfragment orientational anharmonicity.

D. Transformation to center-of-mass separation reaction coordinate

For barrierless reactions the form of the reaction coordinate adopted in the variational determination of the number of accessible states is an important and intricate issue. In this study the direct mapping of the reaction path for singlet ketene fragmentation tacitly assumed a bond-length (R_{CC}) reaction coordinate. Nonetheless, transformation of the resulting path, dissociation potential, and orthogonal force field to corresponding parametrizations for alternative reaction coordinates is necessary to overcome limitations of the R_{CC} representation of the dividing surface. This need is highlighted by considering dissociation energies near threshold, which involves transition states far out on the fragmentation surface. In the enumeration of states, vibrational frequencies in the conserved-mode space should properly be determined by fixing the R_{CC} reaction coordinate and performing a reduced vibrational analysis, as described below. However, constraining the C–C distance rather than the CH_2/CO fragment center-of-mass separation (R_{COM}) engenders long-range kinetic coupling between translation along the reaction coordinate and intrafragment vibrations. In the case of the C–O stretch, the asymptotic effective mass for the vibration becomes roughly that of oxygen instead of the reduced mass of free carbon monoxide. Thus, even at infinite separation the conserved-mode C–O stretching frequency is over 300 cm^{-1} smaller than the free diatomic value, a predicament averted by the use of R_{COM} rather than R_{CC} as the reaction coordinate.

The $R_{CC}\rightarrow R_{COM}$ transformation of the reaction path was accomplished by considering relaxations of the QZ(2*d*1*f*,2*p*1*d*) CCSD(T) optimized reference structures for R_{CC}=2.2, 2.5, 2.8, and 3.1 Å. A local representation of the potential energy surface around each reference point was obtained by assembling the QZ(2*d*1*f*,2*p*1*d*) CCSD(T) force on R_{CC} with the QZ(2*d*,2*p*) CCSD quadratic (Table VI) and by-product semidiagonal (F_{iij}) cubic force constants. The energy of each local representation was then minimized under the constraint of fixed R_{COM}, providing the transformed reference structures given in Table VIII.[80] In the relaxation process, R_{CC} contracts by 0.018–0.023 Å, but as expected the conserved-mode changes are hardly noticeable, except perhaps in the R_{CC}=2.2 Å case (cf. Tables II and VIII). The salient features of the R_{COM} reaction path in this region as

TABLE VIII. Ketene fragmentation path data for center-of-mass reaction coordinate.[a]

	R_{COM} (Å)			
	2.8262	3.1219	3.4189	3.7156
R_{CC}	2.1771	2.4772	2.7814	3.0823
r_{CO}	1.1398	1.1349	1.1340	1.1340
t_{CH}	1.1090	1.1103	1.1101	1.1101
α_{HCH}	103.41	101.84	101.67	101.66
δ_{CCO}	167.17	170.77	171.30	171.56
γ_{CH_2}	−87.86	−91.17	−94.99	−97.22
ΔE_{rlx} (cm^{-1})[b]	−159.7	−69.2	−27.5	−14.7
ω_1	2918	2910	2912	2912
ω_2	2103	2159	2169	2170
ω_3	1386	1411	1422	1426
ω_7	2995	2979	2979	2979
ω_5	959	774	578	422
ω_6	264	171	122	93
ω_8	834	602	411	276
ω_9	218	178	128	104

[a]Bond lengths in Å, bond angles in degree (°), and harmonic frequencies in cm^{-1}. See also footnote a of Table II. In contrast to Table VII, the tabulated vibrational frequencies were extracted from a reduced dimensionality procedure involving Eq. (4) of the text with R_{COM} as the constrained reaction coordinate.
[b]Energy of relaxation relative to reference optimum configuration of bond-length reaction coordinate path.

compared to its R_{CC} counterpart are the straightened C–C–O framework (δ_{CCO} increased by roughly 8°) and the retarded methylene b-axis rotation ($-\gamma_{CH_2}$ diminished by 1.4°–3.5°). The energies of relaxation (ΔE_{rlx}) from the R_{CC} reference structures range from 0.04 to 0.46 kcal mol^{-1} (Table VIII), or only 1.7–3.3 % of the corresponding $CH_2\cdots CO$ binding energies. Therefore, the R_{COM} dissociation potential was obtained simply by appending the ΔE_{rlx} corrections to the final ΔE_e values derived in Table V.

Once the R_{COM} reference structures were obtained, the QZ(2d,2p) CCSD quadratic force constants in Table VI were corrected slightly for the $R_{CC}\rightarrow R_{COM}$ relaxation of the geometry on the basis of the associated semidiagonal cubic force field. The resulting quadratic force field was then transformed with the aid of INTDER (Ref. 81) to a new representation in which internal coordinate S_4 was set to R_{COM}. The reduced vibrational analysis described below, whereby R_{COM} is constrained, yielded the harmonic frequencies listed in Table VIII. Unlike the R_{CC} case, the C–O stretch (ω_2) now decays rapidly toward ω_e of free carbon monoxide (2170 cm^{-1}), and all conserved-mode frequencies are within 15 cm^{-1} of their asymptotic values by R_{COM}=3.12 Å (R_{CC}=2.48 Å). The R_{COM} frequencies are also in qualitative agreement with the interpretive frequencies of Table VII, which were derived from a vibrational procedure of full dimensionality.[79] The most significant distinctions in the ω_i sets are that in the R_{COM} case there is slower decay of ω_6 and ω_9 to zero and a smaller ω_2 value near R_{CC}=2.2 Å.

IV. TRANSITION-STATE NUMBER OF STATES

A. Decoupling of conserved and transitional modes

An assumed separation of modes into conserved vibrational modes, correlating with the internal vibrations of the $^1CH_2$ and CO fragments, and transitional modes, correlating with the relative and overall rotations of these two fragments, has provided the basis for many of the recent theoretical treatments of barrierless reactions. The near independence of the conserved-mode quadratic force field on the value of the reaction coordinate (*vide supra*) suggests that such a separation of modes should also prove useful here. However, before implementing such a separation it is important to consider the details of the evaluation of the conserved-mode vibrational frequencies and particularly their dependence on the assumed *form* for the reaction coordinate.

The general expression for the energy-resolved number of states may be written as[82]

$$N_E(R)=\frac{1}{h^n}\int d\mathbf{q}'\,d\mathbf{p}'\,\Theta[E-T^{\ddagger}(R,\mathbf{q}',\mathbf{p}')-V(R,\mathbf{q}')], \tag{3}$$

where Θ is the Heavyside step function, $\mathbf{q}'$ includes all $n+1$ coordinates except the reaction coordinate R, and $\mathbf{p}'$ is the corresponding conjugate momentum vector. The reduced kinetic energy $T^{\ddagger}$ involves the space spanned by $\mathbf{q}'$ and is given by

$$T^{\ddagger}=\tfrac{1}{2}\mathbf{p}'^{\dagger}\mathbf{G}^{\ddagger}\mathbf{p}'=\frac{1}{2}\sum_{i,j=1}^{n}\left(g_{ij}-\frac{g_{i,n+1}g_{j,n+1}}{g_{n+1,n+1}}\right)p_ip_j, \tag{4}$$

where the g_{ij} are standard G-matrix elements[83] in the full space, and the reaction coordinate corresponds to coordinate $n+1$.

The expression for $N_E(R)$ given by Eq. (3) provides a starting point for implementing various approximations such as the rigid-rotor, harmonic-oscillator model or alternatively the assumed separation of conserved and transitional modes. In particular, evaluating $\mathbf{G}^{\ddagger}$ for a reference geometry such as the minimum energy structure for a given value of R and employing a quadratic expansion of V yields a rigid-rotor, harmonic-oscillator expression for N_E. Alternatively, an approximate separation into conserved modes and transitional modes may be obtained by first separating $\mathbf{G}^{\ddagger}$ into blocks corresponding to the conserved and transitional modes, and then neglecting the coupling between these blocks. In turn, the potential may be written as

$$\begin{aligned}V(R,\mathbf{q}_c,\mathbf{q}_t)=&V_{\text{rxn path}}(R,\mathbf{q}_c^e,\mathbf{q}_t^e)+\Delta V_{\text{conserved}}(R,\mathbf{q}_c,\mathbf{q}_t^e)\\&+\Delta V_{\text{transitional}}(R,\mathbf{q}_c^e,\mathbf{q}_t)\\&+V_{\text{coupling}}(R,\mathbf{q}_c,\mathbf{q}_t),\end{aligned} \tag{5}$$

where $\mathbf{q}_c$ and $\mathbf{q}_t$ denote the conserved and transitional mode coordinates, respectively, and the e superscripts denote R-dependent optimized structural parameters. Neglecting V_{coupling} in the potential then facilitates the separation of the full Hamiltonian into a conserved-mode Hamiltonian and a transitional-mode Hamiltonian.

In the present treatment, the conserved modes are separated out and described by a quadratic expansion of the potential. The rigid-rotor, harmonic-oscillator energy levels obtained entirely in the conserved-mode space are generally within a few cm^{-1} of those obtained in the corresponding analysis of the full reduced Hamiltonian,[84] thereby suggesting the validity of neglecting the couplings between the conserved and transitional modes in both the reduced G-matrix and the potential. However, it must be recognized that the conserved-mode block of $\mathbf{G}^{\ddagger}$ is itself dependent on the orientational coordinates, and this coupling is not always negligible. Similarly, the transitional mode block of $\mathbf{G}^{\ddagger}$ depends to some extent on the conserved-mode coordinates, but insofar as the conserved-mode coordinates generally experience only a minor excursion from their equilibrium values, such coupling is relatively unimportant and has been neglected here.

An important aspect of any variational transition-state theory study involves the form of the assumed reaction coordinate. Studies of some related reactions have suggested that a bond-length reaction coordinate, R_{CC} here, should provide a good first approximation to the optimum reaction coordinate in the inner transition-state region within the variable reaction coordinate framework.[85] However, at larger separations the center-of-mass separation distance R_{COM} is

the preferred reaction coordinate. In the analysis to follow both bond-length and center-of-mass separation reaction coordinates will be explicitly considered.

For the R_{COM} case the conserved-mode frequencies are generally within a few cm^{-1} of the corresponding CO and $^1CH_2$ fragment rigid-rotor, harmonic-oscillator values. Furthermore, the conserved-mode block of the reduced G-matrix is independent of the transitional-mode coordinates. As a result, the number of transitional-mode states N_T for a specific conserved-mode vibrational state $\mathbf{v}_C$ may be written as

$$N_T(E,\mathbf{v}_C,R_{\mathrm{COM}})=N_T[E-E_{\mathbf{v}_C}(R_{\mathrm{COM}},\mathbf{q}_t^e)]$$
$$=\int d\mathbf{q}_t d\mathbf{p}_t \Theta[E-E_{\mathbf{v}_C}(R_{\mathrm{COM}},\mathbf{q}_t^e)-H_t], \tag{6}$$

where H_t is the transitional-mode Hamiltonian which depends explicitly on the coordinates $\mathbf{q}_t$ and their conjugate momenta $\mathbf{p}_t$.

For the R_{CC} case the conserved-mode frequencies resulting from the reduced G-matrix analysis at 3.1 Å are 2910, 1867, 1425, and 2979 cm^{-1} for modes 1–3 and 7, respectively. Similar values are obtained for the remaining C–C separations. The $^1CH_2$ R-dependent frequencies are again close to the separated fragment frequencies, or at least for the R-dependent optimized structures. However, the CO stretching frequency of the R-dependent optimized structures is generally about 300 cm^{-1} below the separated CO frequency, as mentioned in Sec. III D. Full vibrational analyses which employ a force constant matrix with the C–C stretching force constant set to infinity yield numerically identical values for these frequencies. This large decrease in the CO stretching frequency results in the available energy being substantially greater than in the corresponding case of the R_{COM} reaction coordinate. This difference in the available energy for a given vibrational state has important implications for the form of the optimum reaction coordinate.

Importantly, within the bond-length reaction coordinate framework each of the conserved-mode frequencies is also strongly dependent on the specific transitional-mode coordinates (varying at least 100 cm^{-1}) due to the dependence of the reduced G-matrix elements themselves on these coordinates.[86] This strong dependence of the conserved-mode frequencies on the transitional-mode coordinates suggests that the transitional-mode number of states for a specific conserved-mode vibrational state should be written as

$$N_T(E,\mathbf{v}_C,R_{\mathrm{CC}})=\int d\mathbf{q}_t d\mathbf{p}_t \Theta[E-E_{\mathbf{v}_C}(R_{\mathrm{CO}},\mathbf{q}_t)-H_t], \tag{7}$$

where now the vibrational energy $E_{\mathbf{v}_C}$ is to be evaluated for each separate orientation. Sample evaluations indicate that the neglect of the orientational dependence of $E_{\mathbf{v}_C}$ results in an overestimate which is typically on the order of 10%, but is occasionally as large as 50%.

For simplicity the above discussion has centered on the evaluation of the energy-resolved number of states. In actuality, the present calculations have focused on the evaluation of the energy- and angular momentum–resolved number of states $N_{EJ}(R)$. The procedures described above generalize to this case by replacing $N_T(E)$ with $N_T(E,J)$, with the algorithm described in Ref. 87 allowing the evaluation of the latter quantity. The basis of this algorithm is identical to that described earlier in Ref. 88, differing solely in the use of a more efficient integration procedure. Importantly, the low-frequency nature of these transitional modes implies that there should be little error in employing a classical treatment for them.[24,89] Meanwhile, the conserved modes are treated quantum mechanically via the implementation of quantum harmonic oscillator expressions for $E_{\mathbf{v}_C}$.

B. Vibrational adiabaticity and $N_{EJ}^{\dagger}$

The evaluation of the full transition-state number of states $N_{EJ}^{\dagger}$ must involve a summation over each of the conserved-mode vibrational states and a minimization with respect to the *form* and the *value* of the reaction coordinate. Two separate and ultimately different schemes for convoluting in the conserved modes are appropriate under different circumstances. In particular, if the motions in the conserved-mode vibrations are strongly mixed leading to rapidly equilibrating statistical distributions within the transition state region, then $N_{EJ}^{\dagger}$ should be evaluated as

$$N_{EJ}^{\dagger}(\mathrm{statistical})=\min\left[\sum_{\mathbf{v}_C} N_T(E,\mathbf{v}_C,J,R);R\right]. \tag{8}$$

Alternatively, if the conserved-mode quantum numbers are nearly adiabatic during the motion from the transition state on to separated fragments, then $N_{EJ}^{\dagger}$ should be evaluated as

$$N_{EJ}^{\dagger}=\sum_{\mathbf{v}_C} N_T^{\dagger}(E,\mathbf{v}_C,J), \tag{9}$$

where $N_T^{\dagger}$ is the minimum of $N_T(R)$ with respect to R. A number of recent comparisons of predicted and observed product vibrational excitation probabilities have provided substantial evidence for the conservation of the vibrational quantum numbers $\mathbf{v}_C$ during the motion from the transition-state region on to separated products for this and related reactions.[8,23,85] Thus, in the present calculations, $N_{EJ}^{\dagger}$ is evaluated within this vibrationally adiabatic, conserved-mode approach, i.e., from Eq. (9).

The presence of minor variations in the vibrational energies $E_{\mathbf{v}_C}$ with R (and just as importantly the strong orientational dependence of $E_{\mathbf{v}_C}$) implies that the explicit evaluation of $N_{EJ}^{\dagger}$ from Eq. (9) requires the determination of an optimum number of states $N_T^{\dagger}(E-E_{\mathbf{v}_C})$ for each specific vibrational state. Unfortunately, such an evaluation is quite time-consuming for the highest energies due to the accessibility of 20 or more conserved-mode vibrational states. Thus, some simplifications were introduced which result in minor but gradually increasing uncertainties as the excess energy increases. In particular, $N_T^{\dagger}$ was only evaluated explicitly for

the ground vibrational state. An estimate for $N_T^\dagger$ for the higher vibrational states was then obtained as the value for the ground state at the available energy given as $E - E_{\mathbf{v}_C}(\infty)^{\text{expt}} + E_{\mathbf{0}}(\infty)^{\text{expt}}$ or $E - E_{\mathbf{v}_C}(\infty)^{\text{expt}} + E_{\mathbf{0}}(\infty)^{\text{expt}} + (v_{\text{CO}} + \frac{1}{2})\ 290\ \text{cm}^{-1}$ for the R_{COM} and R_{CC} reaction coordinates, respectively, where $E_{\mathbf{0}}(\infty)$ is the ground-state vibrational energy of the separated fragments. This expression allows for the direct inclusion of anharmonic effects via the incorporation of experimental estimates for the energies of the vibrational states, with those for CO and $^1CH_2$ ($E_{\mathbf{v}_C}^{\text{expt}}$) obtained from Refs. 68 and 77, respectively. The $^1CH_2$ experimental vibrational energies for some of the higher-lying, but still accessible, states are not available. For these few states the theoretical values from the fit denoted IB in Ref. 74 were employed instead.

These expressions completely neglect the R and orientational dependence of the vibrational energies for all but the ground vibrational state. For both the R_{CC} and R_{COM} reaction coordinates, the R dependence is weak and thus its neglect seems reasonable. Furthermore, there is essentially no orientational dependence to the vibrational energies for the R_{COM} reaction coordinate. However, for the R_{CC} reaction coordinate, the conserved-mode vibrational energies do depend strongly on the transitional-mode coordinates, being substantially smaller in general than the value for the optimum structure. As a result, the use of what amounts to roughly the optimal-structure energy shift somewhat overestimates the available energy and thereby the value for $N_T^\dagger(\mathbf{v}_C)$ for the excited vibrational states. However, the excited vibrational states themselves make only a relatively minor contribution to the full $N_{EJ}^\dagger$. Rough estimates suggest that the resulting values for $N_{EJ}^\dagger$ may be at most a 5–10% overestimate at the highest energies considered here. In summary, while the direct inclusion of this orientational dependence is feasible via the direct evaluation of harmonic-oscillator based estimates for the vibrational energies (and perhaps including further anharmonicity corrections), it would be quite time-consuming and was deemed unnecessary here.

C. Direct statistics

The Monte Carlo based evaluation of $N_T(R)$ and thereby $N_T^\dagger$ for the ground conserved-mode vibrational state requires explicit values for the interaction energy between the $^1CH_2$ and CO fragments for arbitrary orientations at R_{CC} separations of about 2–3 Å (or equivalently R_{COM} between 3 and 4 Å). In Ref. 24, separate analytic potentials describing these interactions were developed for R_{CC} values of 2.2, 2.5, 2.8, and 3.1 Å. These four separate four-dimensional analytic potentials were based on fits of Fourier series expansions in the transitional-mode coordinates to the quantum chemical data obtained at the MP2/6-31G* level. The difficulties and uncertainties in obtaining accurate multidimensional potentials has led us to consider an alternative approach to estimating the effects of anharmonicities on the number of states. In particular, we have recently noted that the phase space integrals involved in the evaluation of $N_T(R)$ are often reasonably well converged after only a limited number (e.g., about 100) of configurational samplings. This rapid convergence suggests the feasibility of directly determining the interaction energies from *ab initio* quantum chemical calculations at each of the sampled configurations.

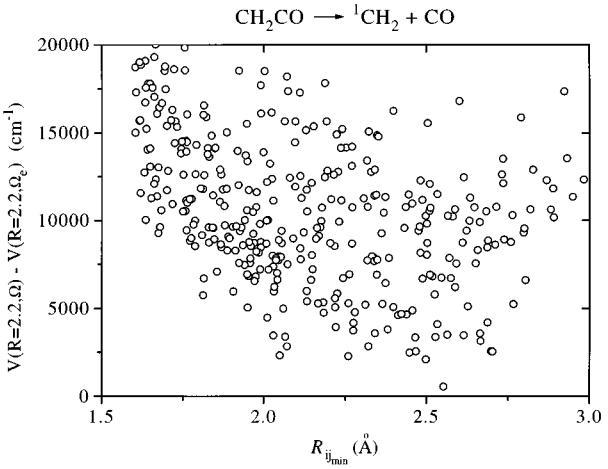

FIG. 8. Plot of the MP2/6-31G* calculated interaction energies for the configurations sampled during the phase space integration as a function of $R_{ij_{\min}}$, the minimum nonbonded interfragment separation distance.

An important aspect of the implementation of this ''direct statistics'' appoach is, of course, the minimization of the number of calls to the potential. A detailed description of the validity and efficiency of direct statistics approaches for studying the kinetics of barrierless reactions will be presented in Ref. 90. Here, two key aspects are briefly described which allow for the generation of a minimal number of configurations. First, the momentum and configurational integrals are sampled separately. With this separation it is possible to accurately sample over momentum space for each configuration that is generated, thereby removing any contribution from the momentum integrals to the integration uncertainties. The second aspect involves the recognition that if any two nonbonded atoms are very close to one another the potential energy will be so large and repulsive that this configuration will make no contribution to the integral. Correspondingly, it should be possible to reject such configurations prior to the generation of *ab initio* quantum chemical estimates for their interaction energies.

In this application, a simple procedure for rejecting such configurations based solely on the minimum separation between any two nonbonded atoms on separate fragments was employed. In particular, plots of the interaction energy versus the minimum nonbonded interfragment separation for each individual configuration were made for a preliminary 100-point sampling. These plots provide an indication of the minimum energy that might be expected as a function of the minimum nonbonded interfragment interatomic distance. A sample plot for $R_{\text{CC}}=2.2$ Å is given in Fig. 8, which includes the first 1000 configurations sampled. The distribution of points suggests that any configuration which has a minimum nonbonded interfragment distance of 1.7 Å or less will have an energy which is at least 10 000 cm^{-1} above that of the optimum orientation, and thus, by conservation of energy, it

TABLE IX. Transitional-mode number of states $N_T(E,J=0,\ R)$ for singlet ketene fragmentation.[a]

Excess energy (cm^{-1})	R_{CC} (Å)			
	2.2	2.5	2.8	3.1
50	(1.3, 1.6)	(0.55, 0.36)	(0.24, 0.16)	(0.20, 0.11)
70	(1.4, 1.6)	(0.57, 0.37)	(0.25, 0.17)	(0.22, 0.13)
100	(1.4, 1.7)	(0.61, 0.40)	(0.27, 0.20)	(0.25, 0.16)
140	(1.4, 1.7)	(0.62, 0.44)	(0.30, 0.24)	(0.30, 0.22)
200	(1.5, 1.9)	(0.68, 0.52)	(0.36, 0.31)	(0.39, 0.33)
300	(1.6, 2.1)	(0.78, 0.67)	(0.46, 0.50)	(0.60, 0.64)
450	(1.9, 2.5)	(0.94, 1.00)	(0.67, 0.96)	(1.04, 1.4)
700	(2.3, 3.4)	(1.3, 1.9)	(1.2, 2.4)	(2.2, 3.6)
1000	(2.8, 4.8)	(1.8, 3.7)	(2.2, 5.3)	(4.5, 7.8)
1400	(3.8, 7.4)	(2.9, 7.6)	(4.3, 12)	(9.3, 16)
2000	(5.6, 14)	(5.3, 18)	(9.7, 26)	(21, 34)
3000	(10, 31)	(12, 47)	(26, 66)	(52, 81)
4500	(21, 81)	(34, 123)	(67, 160)	(129, 189)
6000	(40, 162)	(73, 241)	(133, 298)	(241, 342)

[a]The entries in parentheses are $N_T(R)\times 10^{-3}$ values for the R_{CC} and R_{COM} reaction coordinates, in order. The R_{COM} results are tabulated according to the reference value of R_{CC} employed in the reaction path determination.

cannot make any contribution to $N_T(E)$ for the energies of interest here. Therefore, such configurations were rejected prior to any *ab initio* quantum chemical determinations. More sophisticated and efficient methods for estimating the feasibility of rejection are possible, as will be described in Ref. 90. However, the present procedure is simple, straightforwardly implemented, and easily of sufficient efficiency here.

The orientational dependence of the interaction energies in these direct statistics calculations was evaluated at the MP2/6-31G* level for each of the four C–C bond lengths. These relative interaction energies were then added to the R_{CO}-dependent optimum interaction energies determined in the focal-point analysis to provide absolute data in the direct statistics evaluations. The direct statistics results were based on Monte Carlo samples of 2000 configurations, which typically corresponded to about 1000 actual energetic determinations (requiring about 1 CPU day on a Silicon Graphics Indigo workstation). For each energetically accessible configuration, 500 separate momentum points were sampled. The total 1σ sampling error bars then ranged from about 30% to about 5% with the typical value being around 10% for the R value most closely corresponding to $R^\dagger$. The maximum sampling uncertainties occur for low energies and short separations where relatively few configurations contribute.

Again, this MP2/6-31G* based approach is very reasonable due to the good agreement observed between the MP2/6-31G* and CCSD/QZ($2d$,$2p$) force constants. The sole nonnegligible difference in these force constants of a factor of 1.5 for the torsional mode was accounted for explicitly in the final analysis, as described below. Note, however, that at the harmonic level this difference in force constants would yield a difference of only 22% in the estimated force constants. An important question is to what degree the results depend on the accuracy of the MP2/6-31G* estimates of the anharmonic effects. One indication of the extent of the dependence on anharmonic effects is provided by a comparison of the results obtained via the implementation of the quadratic force field for the potential within the phase space integrations with those obtained from the direct statistical analysis. For the bond-length reaction coordinate the maximum deviation between such calculations was found to be about a factor of 2 for moderately high energies at a separation of 3.1 Å. More typically the two calculations were found to agree to within the sampling error bars, particularly, for separations close to the transition state separations for a given E. Thus, while MP2/6-31G* calculations may not provide an extremely accurate estimate of the anharmonic energies, the analysis suggests that the anharmonic effects on $N_T^\dagger$ are probably about 40% or less for this reaction.

A similar direct statistical analysis was performed for the R_{COM} reaction coordinate case. However, in this instance, it was found that very few configurations (i.e., typically less than 1%) could be *a priori* rejected. This difference in the number of configurations that may be rejected prior to any energetic determination suggests that the configurational integral will be much smaller for the bond-length reaction coordinate. This reduced rejection probability for R_{COM} is thereby indicative of why the bond-length reaction coordinate is expected to provide a better approximation to the true reaction coordinate at shorter separations, where differences due to the kinetic factors are relatively unimportant.

D. Results for $N_T^\dagger(E,J)$

The direct statistics determinations of $N_T(E,J=0,\ R)$ are reported in Table IX for both the bond-length and center-of-mass separation reaction coordinates. From these $N_T(E,J,R)$ data, final estimates for $N_T^\dagger$ for the inner transition-state region were obtained via a quadratic fit to the number of states determined for three of the four R values at each E, as reported in Table X. Included in these final estimates for $N_T^\dagger$ are corrections (by a factor of 1.00 to 1.23) for the overestimation of the torsional force constant at the MP2/6-31G*

TABLE X. Optimized transitional mode number of states (N_T^+) and transition-state locations ($R^\dagger$).[a]

Excess energy (cm^{-1})	CC	COM	CC, RRHO	COM, RRHO	PST[b]
50	(0.18, 2.99)	(0.11, 3.67)	(0.08, 3.10)	($\leqslant$0.02, ex)[c]	0.029
70	(0.20, 2.98)	(0.13, 3.66)	(0.09, 3.10)	($\leqslant$0.03, ex)[c]	0.050
100	(0.23, 2.97)	(0.16, 3.64)	(0.10, 3.10)	($\leqslant$0.03, ex)[c]	0.092
140	(0.28, 2.95)	(0.21, 3.60)	(0.12, 3.10)	($\leqslant$0.03, ex)[c]	0.20
200	(0.35, 2.92)	(0.31, 3.54)	(0.15, 3.08)	($\leqslant$0.04, ex)[c]	0.40
300	(0.51, 2.86)	(0.55, 3.43)	(0.20, 3.05)	(0.06, 3.73)	0.90
450	(0.76, 2.78)	(1.0, 3.29)	(0.31, 2.97)	(0.10, 3.70)	2.1
700	(1.3, 2.68)	(2.2, 3.20)	(0.55, 2.86)	(0.21, 3.59)	5.1
1000	(2.2, 2.57)	(4.5, 3.09)	(0.90, 2.72)	(0.38, 3.42)	10
1400	(3.4, 2.47)	(8.5, 2.96)	(1.4, 2.62)	(0.62, 3.25)	20
2000	(5.6, 2.37)	(15, 2.71)	(2.7, 2.53)	(1.2, 3.20)	41
3000	(11, 2.28)	($\leqslant$35, ex)[c]	(5.8, 2.41)	(2.7, 3.09)	92
4500	(23, 2.17)	($\leqslant$89, ex)[c]	(13, 2.30)	(6.4, 2.99)	⋯
6000	(36, 1.99)	($\leqslant$175, ex)[c]	(24, 2.26)	(12, 2.93)	⋯

[a]The entries in parentheses are $N_T^\dagger \times 10^{-3}$ and $R^\dagger$ (Å) values, in order. The CC and COM columns are obtained using R_{CC} and R_{COM} reaction coordinates, respectively; RRHO denotes rigid-rotor, harmonic-oscillator estimates.

[b]Number of states given by phase-space theory (PST) applied to separated products.

[c]Cases in which the quadratic interpolation procedure yields a transition state external (ex) to the region spanned by the high-level reaction path computations. The limit for the number of states is thus obtained from the relevant boundary point.

level (*vide infra*). The quadratic fitting procedure leads to $N_T^\dagger$ values which are within 15% of the minimum $N_T(E,J,R)$ among the four reference R_{CC} values. Also given in Table X are the inner transition-state locations obtained from the quadratic fitting procedure. For R_{CC} these estimates are seen to vary continuously from about 3.0 to 2.2 Å for excess energies ranging from threshold up to 4500 cm^{-1}, with $R_{CC}^\dagger$ decreasing with increasing energy. Similarly, R_{COM} varies from about 3.8 to 2.7 Å for the same range of excess energies. The reaction path determinations span this region, and thus no extrapolations are required except perhaps for the very highest and lowest energies.

Phase space theory (PST),[25] in which the energetics of the transition state are assumed to be simply those of the product fragments coupled with effective orbital barriers, has long provided an important reference theory for analyzing barrierless reactions. Thus, for comparison purposes alone we have also presented PST estimates for the energy dependence of the transitional-mode number of states in Table X. These PST calculations correspond to quantum mechanically based determinations of the number of available states in the limit of infinite separation.

At the lowest energies the PST number of states is smaller than each of the present R-dependent direct statistical evaluations for the inner transition-state region, implying that an outer transition state lies at separations greater than the maximum of 3.1 Å considered in the variational calculations. The PST number of states then provides a good first estimate for the reactive flux at these low energies. However, at an energy of about 140 cm^{-1}, $N_T^\dagger$ for the R_{COM} reaction coordinate becomes smaller than the PST number, and thus the variationally determined inner transition state becomes the dominant one. With increasing energy the inner transition-state variational RRKM result, given by the smaller of the $N_T^\dagger$ values for the R_{COM} and R_{CC} reaction coordinates, diverges to an increasing extent from the PST prediction. Furthermore, the best reaction coordinate for this inner transition-state region switches from R_{COM} to R_{CC} at an energy of about 260 cm^{-1}. At the highest energies considered here, the bond-length variational results are a factor of nearly 10 lower than the PST results and also a factor of 4 lower than the R_{COM} results. These large differences indicate the extent of the reduction in the available phase space due to the strong interfragment repulsions in the inner transition-state region. Clearly these repulsions play an important role in the kinetics of the ketene dissociation process.

RRKM models based on rigid-rotor, harmonic-oscillator (RRHO) assumptions for the energy levels in the transition-state region have also been commonly applied to the study of the kinetics of these reactions. Thus, we also report in Table X RRHO results for both the R_{COM} and the R_{CC} reaction coordinate cases. As is commonplace, quantum estimates for the vibrational energies were employed. However, note that the implementation of classical state counting procedures for the transitional modes, in analogy with the present phase space integral methodology, results in deviations of less than 10% from these quantum estimates. Interestingly, these RRHO predictions substantially underestimate the variationally optimized direct statistical results, with the R_{CC}- and R_{COM}-based RRHO values typically being factors of 2 and 4–9 too low, respectively. These large differences clearly illustrate the inaccuracies that may arise when rovibrational coupling and anharmonicity are neglected. Recalling that the quadratic force field phase space integral values agreed reasonably well with the direct statistics results, the error seems primarily due to strong kinetic couplings of the intermolecular vibrational modes.

As mentioned above, the present bond-length calculations have evaluated the conserved-mode zero-point energy for each orientation sampled in the transitional-mode phase space integrals. We have also performed related calculations in which the conserved-mode vibrational frequencies are taken as either (i) those evaluated for the R-dependent optimized structures or (ii) the standard fragment vibrational frequencies. At the highest energies the estimates for $N_T^\dagger$ from both of these approaches reduce to that obtained employing the orientation-dependent frequencies. This similarity is an indication of the insignificance of variations of a few hundred cm^{-1} in the total energy when its value is on the order of 10 000 cm^{-1}. In contrast, at the lowest energies the first approach gives $N_T^\dagger$ 50% greater than the orientation-dependent result, whose underlying frequencies are on average somewhat higher than those of the optimum structure. Meanwhile, the second approach, employing the fragment vibrational frequencies, yields $N_T^\dagger$ 50% lower than the orientation-dependent result since the fragment frequencies tend to be somewhat higher than those obtained from the reduced G-matrix analysis.[91]

To a first approximation one might expect the deficiency in the MP2/6-31G* torsional curvature to lead to disparities in the number of states proportional to the square root of the torsional force constant error. However, this predicted overestimate of 22% is too large at high energies since the torsional motion is of a hindered rotor nature, for which the force constant plays a negligible role in the limit of infinite energy. An alternative torsional correction procedure involves the implementation of a revision of the MP2/6-31G* based model potential employed in Ref. 24. With this procedure the model potential is altered to reproduce the current focal-point energies and either the CCSD/QZ($2d$,$2p$) or MP2/6-31G* force constants for the R-dependent optimum structures, while retaining the functional form given in Ref. 24. The comparison of the number of states obtained for the two different force constant sets then provides an estimate of the error introduced in the direct statistical analysis by directly employing the MP2/6-31G* values. Interestingly, the number of states given by the model potential is generally a factor of 1.8 times that obtained in the ''direct statistics'' analysis, thereby suggesting that the analytical potential of Ref. 24 does not provide a very accurate representation of the orientational dependence of the interaction energies at the MP2/6-31G* level. Thus, the comparative MP2/6-31G* correction factor, which corresponds to at most a 22% increase, may also be somewhat inaccurate, but it was directly incorporated in the final direct statistics results for $N_T^\dagger$ reported in Table X.

V. REACTANT DENSITY OF STATES

The density of states for the reactants, ρ_{EJ}, is another important component of the RRKM theory expression for the rate constant. The previous applications of RRKM theory to this reaction have employed a simple rigid-rotor, harmonic-oscillator estimate for this density of states.[22,24] However, the combination of the small size and large dissociation energy for CH_2CO suggests that anharmonic effects may be of considerable importance. Furthermore, in their recent studies of the triplet dissociation of ketene, Moore and co-workers have suggested that the density of states for the reactant is either two[15] or four[16] times that evaluated at the rigid-rotor, harmonic-oscillator limit. Here a detailed theoretical analysis of the predicted anharmonic effects on the density of states is undertaken as a means to help resolve the outstanding uncertainty in ρ_{EJ}.

The basis of the present estimate of ρ_{EJ} is the implementation of second-order perturbation theory to obtain anharmonic vibrational energy levels from a quartic force field derived in a companion high-level quantum chemical study.[27] A brief review is given here of the procedures involved in the determination of this scaled quantum mechanical quartic force field, with a more detailed description being given in Ref. 27. The quadratic force field was first determined at the CCSD/QZ($2d$,$2p$) level employing reference CCSD(T)/QZ($2d1f$,$2p1d$) geometries. The cubic and quartic force constants were then determined at the MP2/QZ($2d$,$2p$) level of theory. Minor adjustments in the geometries and quadratic force constants then provided a reference quartic force field for which the application of spectroscopic perturbation theory reproduced the experimental transition frequencies to within 3 cm^{-1} for CH_2CO and various of its isotopomers.

A straightforward procedure for estimating the density of states for the reactant from this quartic force field entails the differentiation of the number of available vibrational states for the reactant, $N_{\text{vib,reactant}}$. The latter quantity is determined by the direct summation over the quantum numbers of a step function in the energy minus the state-dependent vibrational energy, $E_{v_1,\ldots,v_9}$:

$$N_{\text{vib,reactants}}(E)=\sum_{v_1,\ldots,v_9}^{N_i^{\max}}\Theta(E-E_{v_1,\ldots,v_9}), \tag{10}$$

where $E_{v_1,\ldots,v_9}$ is determined from standard spectroscopic perturbation theory according to[67,92]

$$E_{v_1,\ldots,v_9}=\sum_i \omega_i(v_i+\tfrac{1}{2})+\sum_{i\geqslant j}\chi_{ij}(v_i+\tfrac{1}{2})(v_j+\tfrac{1}{2}). \tag{11}$$

The number of states obtained from Eq. (10) was fit to the following functional form:

$$\ln N_{\text{vib,reactants}}=f(E)\sqrt{E-E_0}, \tag{12}$$

where

$$f(E)=a+bE+c\ \exp(-dE). \tag{13}$$

Analytic differentiation of this form then provided ρ_{EJ}.

The parameters resulting from the fit of this analytic function to the numerically evaluated number of reactant states are reported in Table XI for frequencies and anharmonicities based on the full anharmonic data reported in Ref. 27 (Method 1), and the underlying quadratic force field (Method

TABLE XI. Parameters in the analytic form for the number of reactant states.[a]

	Method	E_0	a	b	c	d
1	anharm, full	7251.1	0.11488	−3.0326(−7)	−0.28360	3.1109(−4)
2	harmonic	7321.1	0.11669	−3.1886(−7)	−0.30542	3.1638(−4)
3	anharm, no Coriolis	7231.1	0.11611	−2.8581(−7)	−0.29487	3.1621(−4)
4	anharm, $(\chi_{66},\chi_{65})/3$	7251.1	0.11610	−3.0492(−7)	−0.28136	3.1140(−4)
5	anharm, no Coriolis, $(\chi_{66},\chi_{65})/3$	7221.1	0.11733	−2.8056(−7)	−0.28666	3.1368(−4)

[a]See Eqs. (12) and (13); units consistent with vibrational energy (E) in cm^{-1}. Numbers in parentheses denote powers of 10.

2). A sample plot of these fits is provided in Fig. 9, illustrating the excellence of the fitting procedure. Unfortunately, as discussed in Ref. 27, there is some uncertainty in the quartic force field analysis regarding the contribution to the off-diagonal anharmonicities from the Coriolis interactions and the anharmonic constants involving the b_1 normal modes. As a result, the density of states has also been estimated for three alternative assumptions for the energy levels, as suggested in Ref. 27. In the first alternative (Method 3) the Coriolis contribution to the off-diagonal anharmonicities is neglected. In the second alternative (Method 4) the anharmonicity parameters χ_{66} and χ_{65} are divided by 3. Finally, the above two alternatives have been implemented simultaneously in Method 5. The parameters for each of these three alternatives are also reported in Table XI.

Interestingly, at the singlet dissociation threshold the harmonic density of states is actually 22% greater than that evaluated with the full anharmonicities. Meanwhile, the removal of the Coriolis contributions and reduction of χ_{66} and χ_{65} yields densities of states which are 43 and 23% greater than the full anharmonic density of states. The rate constant calculations reported in the next section employ the density of states evaluated via the neglect of the Coriolis contributions to the off-diagonal anharmonic constants (Method 3), since this provides an intermediate result and furthermore appears most likely to be accurate.

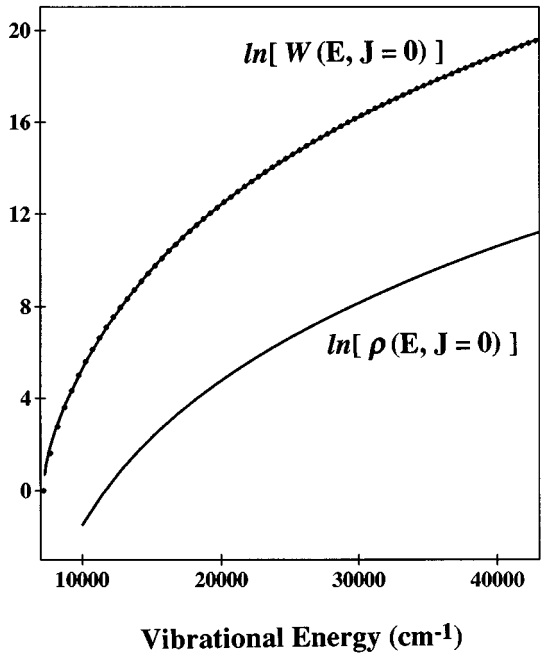

FIG. 9. Plot of the logarithm of the number W and density ρ of states for the reactant CH_2CO as a function of vibrational energy. The full anharmonic force field is employed in making this plot. The reference zero of energy for this plot is the bottom of the potential well. The total zero-point energy is 6821 cm^{-1}.

All of the ρ_{EJ} predictions are more than a factor of 2.2 lower than the values deduced by Moore and co-workers in their analysis of the corresponding triplet state dissociation assuming all of the triplet components are dynamically coupled to the singlet state.[16,18] However, there are some aspects of their modeling that are still somewhat uncertain. In particular, a number of studies[93] have suggested that in a variety of intersystem crossing processes involving planar aromatic species, one of the spin components of the triplet state is often more weakly coupled to the singlet state than the other two components, a crossing rate 50 times smaller being typical. Such observations would suggest that a spin degeneracy of only two might be most appropriate for the triplet ketene data since the intersystem crossing rate itself is only about 100 times the threshold rate. Their estimates are also strongly dependent on the assumed reaction rate at the top of the barrier, or equivalently the height of the steps in the reaction rate constant arising from the opening of a single additional channel in the transition state. Unfortunately, the estimate of this threshold rate constant is not straightforward due to complications arising from tunneling, thermal averaging, and perhaps even resonance fluctuations.[18,94] Indeed, even in their most recent analysis Moore and co-workers are not able to simultaneously model all aspects of the energy dependence near threshold for all of the isotopomers that they have observed. Thus, one additional, but unlikely, possibility is that Moore and co-workers have overestimated this first step by a factor of 2. Higher-level quantum chemical predictions of the lowest energy levels for the triplet transition state may help to resolve these uncertainties.

VI. RATE CONSTANTS

The time-resolved experimental studies of Potter *et al.*[12] have yielded total dissociation rate constants for excess energies ranging from 450 up to 5600 cm^{-1}. The branching ratios determined by Moore and co-workers[7] from 50 up to 2500 cm^{-1} allow for the determination of the individual singlet and triplet dissociation rate constants. Furthermore, Kim *et al.*[7] have used interpolations of their experimentally ob-

served triplet rate constants and singlet-triplet branching ratios to estimate the rate constants for lower excess energies ranging from 56 to 325 cm^{-1}. For energies above 2500 cm^{-1} an estimated singlet yield of 0.75 is employed here in order to obtain singlet dissociation rate constants for comparison with the present calculations.

The experiments have employed cold molecular beams at temperatures of about 3–4 K. Thus, the observed rate constants correspond to a very limited range of total angular momentum values, all near $J=0$. Here, for simplicity, the direct statistical calculations for the inner transition-state region have focused on only $J=0$. Meanwhile, the PST calculations have incorporated a thermal averaging over the rotational states for a temperature of 4 K. This thermal averaging typically results in about a 10% decrease in the rate constant as compared to the $J=0$ rate constant for energies below 100 cm^{-1} and then gradually becomes completely negligible for higher energies. This decrease in the rate constant arises as a result of the presence of a higher threshold for dissociation from the lowest state of ortho ketene as compared to that of para ketene.

One interesting aspect of the earlier variational RRKM studies of this dissociation involved the presence of two well separated transition-state regions. The present direct statistical calculations focus on the determination of the minimum in the number of states for the inner transition-state region (2–3 Å), while PST calculations provide an indication of the number of states for the outer transition-state region. A simple variational RRKM estimate for the dissociation rate constant is then obtained by employing the minimum of these two estimates for $N_{EJ}^{\dagger}$ in Eq. (1). Alternatively, assuming that the two transition states are completely independent with a randomization of the motion in between, an effective number of states N_{eff} should be employed.[95]

$$\frac{1}{N_{\mathrm{eff}}}=\frac{1}{N_{\mathrm{inner}}}+\frac{1}{N_{\mathrm{outer}}}-\frac{1}{N_{\mathrm{max}}}, \tag{14}$$

where N_{inner} and N_{outer} are the inner and outer minima in the number of states, and N_{max} is the maximum in the region separating the two minima.

Here, both the absolute minimum and the effective number of states approaches have been employed in obtaining variational RRKM estimates for the rate constant. For the latter approach, the maximum in the number of states has simply been assumed to be large enough to be of no importance in Eq. (14), which provides a limiting case for the effect of two transition states acting in series. For both approaches the inner minimum is taken as the minimum of the $N_T^{\dagger}$ values evaluated for the bond-length and center-of-mass separation distance reaction coordinates. The resulting estimates for the energy dependence of the singlet dissociation rate constant are reported in Fig. 10 together with the corresponding experimental estimates.[7,12] An expanded view of this plot is provided in Fig. 11.

The overall agreement between the present nonempirical variational RRKM calculations and the experimental measurements is very good. In particular, the effective number of states predictions are generally within 40% of the experimental results, and typically simply overestimate the experimental results by about 25%. The largest deviation of 80% arises at an energy of 3780 cm^{-1}, where the single experimental point falls much lower than any smooth curve through the data. In brief, all disparities are well within the limits of accuracy of the present calculations, particularly since there has been only a limited optimization of the form of the reaction coordinate and since the present estimate of the density of states is expected to gradually degrade as the energy increases. Furthermore, for the highest energies some question remains as to the exact magnitude of the singlet/triplet branching ratios.

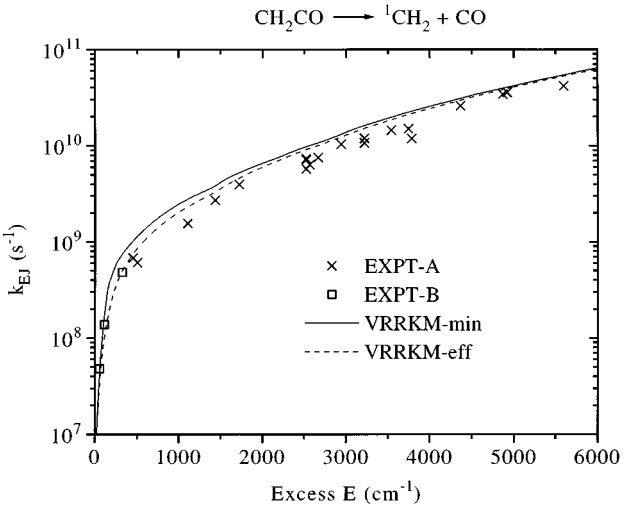

FIG. 10. Plot of the logarithm of the rate constant vs excess energy for the singlet dissociation of ketene. The solid line denotes the absolute minimum of the present direct statistical and PST results, while the dashed line denotes the calculations employing the effective number of states given by Eq. (14). The squares and crosses mark the experimental results of Refs. 7 and 12, respectively.

The expanded view in Fig. 11 indicates a decrease in slope of the rate constant versus energy at an excess energy

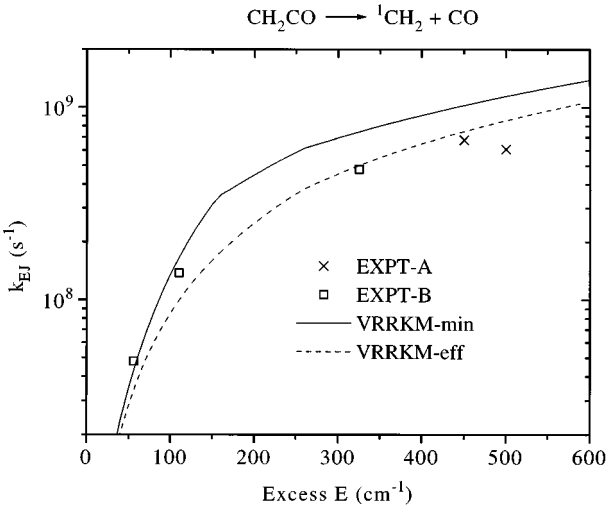

FIG. 11. An expanded view of the plot given in Fig. 10.

TABLE XII. Supplementary material: Total energies (a.u.) along the optimized fragmentation path of singlet ketene.[a]

	6-31G*	QZ(2*d*,2*p*)	QZ(2*d*1*f*,2*p*1*d*)	[13*s*8*p*6*d*4*f*,8*s*6*p*4*d*]
		CH_2CO ($^1A_1$)[R_{CC}=eq]		
RHF	−151.723 386	−151.783 560	−151.789 086	−151.796 956
MP2	−152.147 020	−152.290 891	−152.336 205	−152.368 311
MP3	−152.151 621	−152.292 045	−152.338 774	⋯
MP4	−152.182 105	−152.330 531	−152.377 748	⋯
CCSD	−152.160 697	−152.299 068	−152.343 744	⋯
CCSD(T)	−152.177 417	−152.323 993	−152.370 747	⋯
BD(TQ)	−152.177 137	⋯	⋯	⋯
		$CH_2\cdots CO$ ($^1A'$, R_{CC}=2.2 Å)		
RHF	−151.618 768	−151.681 400	−151.685 069	−151.693 025
MP2	−152.012 451	−152.162 051	−152.202 467	−152.234 247
MP3	−152.025 255	−152.172 960	−152.214 313	⋯
MP4	−152.056 891	−152.212 378	−152.253 777	⋯
CCSD	−152.039 998	−152.185 673	−152.224 862	⋯
CCSD(T)	−152.055 318	−152.209 020	−152.250 116	⋯
BD(TQ)	−152.055 349	⋯	⋯	⋯
		$CH_2\cdots CO$ ($^1A'$, R_{CC}=2.5 Å)		
RHF	−151.615 198	−151.678 033	−151.681 539	−151.689 548
MP2	−152.002 784	−152.151 293	−152.191 170	−152.222 840
MP3	−152.017 188	−152.164 099	−152.204 912	⋯
MP4	−152.047 754	−152.202 229	−152.243 020	⋯
CCSD	−152.032 300	−152.177 425	−152.216 109	⋯
CCSD(T)	−152.046 474	−152.199 305	−152.239 824	⋯
BD(TQ)	−152.046 571	⋯	⋯	⋯
		$CH_2\cdots CO$ ($^1A'$, R_{CC}=2.8 Å)		
RHF	−151.613 308	−151.676 604	−151.680 038	−151.688 101
MP2	−151.998 180	−152.146 254	−152.185 898	−152.217 514
MP3	−152.013 259	−152.159 846	−152.200 431	⋯
MP4	−152.043 395	−152.197 447	−152.237 983	⋯
CCSD	−152.028 811	−152.173 712	−152.212 195	⋯
CCSD(T)	−152.042 553	−152.194 952	−152.235 237	⋯
BD(TQ)	−152.042 693	⋯	⋯	⋯
		$CH_2\cdots CO$ ($^1A'$, R_{CC}=3.1 Å)		
RHF	−151.611 895	−151.675 696	−151.679 102	−151.687 212
MP2	−151.995 418	−152.143 538	−152.183 090	−152.214 667
MP3	−152.010 806	−152.157 472	−152.197 968	⋯
MP4	−152.040 726	−152.194 834	−152.235 271	⋯
CCSD	−152.026 618	−152.171 663	−152.210 073	⋯
CCSD(T)	−152.040 179	−152.192 614	−152.232 809	⋯
BD(TQ)	−152.040 344	⋯	⋯	⋯
		CH_2 ($^1A_1$)+CO [R_{CC}=∞]		
RHF	−151.608 910	−151.673 496	−151.676 863	−151.685 231
MP2	−151.990 667	−152.138 951	−152.178 484	−152.210 147
MP3	−152.006 506	−152.153 368	−152.193 847	⋯
MP4	−152.036 113	−152.190 351	−152.230 775	⋯
CCSD	−152.022 618	−152.167 912	−152.206 325	⋯
CCSD(T)	−152.036 001	−152.188 536	−152.228 725	⋯
BD(TQ)	−152.036 207	⋯	⋯	⋯

[a]All energies determined at the CCSD(T)/QZ(2*d*1*f*,2*p*1*d*) optimum geometries appearing in Table II of the text.

of about 140 cm^{-1} for the solid line describing the absolute minimum curve. At this energy the dominant bottleneck in the reactive flux moves from the outer PST transition state to the inner entropically determined transition state. The key aspect of the earlier modeling[23] of the photofragment excitation (PHOFEX) spectra of Moore and co-workers[8] was simply the energy at which this transition from an outer to an inner transition state occurred. The occurrence of this transition at roughly the same energy as in the modeling study (and also again the accurate reproduction of the rate energy curve) suggests that the implementation of the present results into a vibrationally adiabatic RRKM model would again yield good agreement with the PHOFEX spectra.

Additional deflections occur at excess energies of about 260 and 1400 cm^{-1}, respectively. The decrease in slope at 260 cm^{-1} is an indication of the transition from a R_{COM} to a R_{CC} optimum reaction coordinate. This change in slope would likely be smoothed over if a continuous range of re-

action coordinates were considered. The increase in slope at the excess energy of about 1400 cm^{-1} is an indication of the opening of the first excited HCH bending vibrational channel and again plays an important role in the interpretation of the PHOFEX spectra observed by Moore and co-workers.[8] Similar, but less apparent, deflections arise at the openings of the remaining vibrational states.

It is interesting to contrast the present results with those obtained in the preliminary study solely at the MP2/6-31G* level. The previous MP2/6-31G* results for $N_{EJ}^{\dagger}$ at the inner transition state (with the 71 parameter analytical potential energy surface) range from about 3 times greater than the present results near threshold to about 1.5 times greater for the highest energies. A major contribution to the present decreased estimate at low energies is the decrease in the magnitude of the predicted reaction path attractiveness. In contrast, at the shorter separations, where the transition state lies at higher energies, the difference between the focal-point and MP2/6-31G* calculated reaction path energy is both smaller and less important due to the higher total available energy. The change in force constants makes at most a 23% difference in the calculated N_T values and furthermore actually increases the present estimates as compared with the previous estimates in contrast with the change in reaction path energetics. The remaining major contribution comes from the difference between the direct statistical versus analytical potential based procedures, which contributes a nearly constant factor of 1.8 decrease in the present rate constant estimates.

VII. CONCLUDING REMARKS

The agreement between the present nonempirical calculations and the detailed and wide-ranging experimental results of Refs. 7 and 12 provides strong evidence for the validity of variational RRKM theory for this prototypical barrierless reaction. The direct statistical approach employed in these calculations is efficient and straightforward to implement and should provide a useful means for interpolating, extrapolating, and even predicting rate-energy curves for a variety of barrierless reactions. In continuing work, this direct statistics method will be improved via the development of schemes for further reducing the number of potential calls that are required to obtain converged estimates. It is also worth noting that the present approach involving the coupling of high level evaluations of the reaction path energetics with more modest evaluations of the orientational dependence of the energetics should prove generally useful.[96] The validity of such an approach is founded on the general observation that force constant evaluations are often reasonably accurate even when the corresponding absolute energetics are substantially in error.

The present comparison between the transitional-mode number of states evaluated within the bond-length and center-of-mass separation distance reaction coordinate frameworks provides the most meaningful indication to date of the variation of the form of the reaction coordinate as the transition state moves in to shorter separations. At larger separations R_{COM} clearly provides a better form for the reaction coordinate, while at C–C separations of about 2.8 Å or shorter R_{CC} is preferred. Sample calculations for the bond-length reaction coordinate case suggest the importance of considering the dependence of the conserved-mode frequencies, and more specifically the reduced G matrix, on the transitional-mode coordinates. The large deviations between the variational and PST results illustrate the large reduction in the available phase space caused by the interfragment repulsions at short range. Meanwhile the large deviations between the direct statistics results and the corresponding rigid-rotor, harmonic-oscillator results illustrates the importance of accurately treating mode coupling and anharmonicity effects in barrierless reactions.

An important unresolved issue for the dissociation of ketene regards the difference between the calculated density of states and that estimated from the modeling of the triplet state dissociation. Higher level studies of the energetics in the region of the triplet state[97] may help to resolve this disparity. The validity of employing a quartic force field and spectroscopic perturbation theory for these estimates is also an issue.[98] Interestingly, it may be possible to employ related direct phase space integration methods in resolving the latter uncertainties.

Another interesting issue for the dissociation of ketene regards the recent observation of substantial deviations of the product rotational distributions from PST predictions at higher energies.[10,11] One procedure for studying these deviations might involve the generation of a reasonably accurate analytical potential energy surface for the transitional modes from the *ab initio* data determined here. Vibrationally adiabatic trajectory calculations[99] employing this potential energy surface would then provide an optimal procedure for studying these rotational distributions.

ACKNOWLEDGMENTS

Acknowledgment is made to the National Science Foundation for partial support of this research through Grant No. CHE-9215194 (S.J.K.).

[1] R. A. Marcus, J. Chem. Phys. **20**, 359 (1952); **43**, 2658 (1965).
[2] P. J. Robinson and K. A. Holbrook, *Unimolecular Reactions* (Wiley, New York, 1972); W. Forst, *Theory of Unimolecular Reactions* (Academic, New York, 1973).
[3] R. G. Gilbert and S. C. Smith, *Theory of Unimolecular and Recombination Reactions* (Blackwell Scientific, Boston, 1990).
[4] R. A. Marcus, J. Chem. Phys. **45**, 2630 (1966); W. L. Hase, J. Chem. Phys. **57**, 730 (1972); **64**, 2442 (1976); B. C. Garrett and D. G. Truhlar, J. Chem. Phys. **70**, 1593 (1979); S. N. Rai and D. G. Truhlar, J. Chem. Phys. **79**, 6046 (1983).
[5] W. H. Green, Jr., I.-C. Chen, and C. B. Moore, Ber. Bunsenges. Phys. Chem. **92**, 389 (1988).
[6] I.-C. Chen, W. H. Green, Jr., and C. B. Moore, J. Chem. Phys. **89**, 314 (1988).
[7] S. K. Kim, Y. S. Choi, C. D. Pibel, Q.-K. Zheng, and C. B. Moore, J. Chem. Phys. **94**, 1954 (1991).
[8] W. H. Green, Jr., A. J. Mahoney, Q.-K. Zheng, and C. B. Moore, J. Chem. Phys. **94**, 1961 (1991).
[9] W. H. Green, Jr., C. B. Moore, and W. F. Polik, Annu. Rev. Phys. Chem. **43**, 591 (1992).
[10] I. Garcia-Moreno, E. R. Lovejoy, and C. B. Moore, J. Chem. Phys. **100**, 8890 (1994).

[11] I. Garcia-Moreno, E. R. Lovejoy, and C. B. Moore, J. Chem. Phys. **100**, 8902 (1994).
[12] E. D. Potter, M. Gruebele, L. R. Khundkar, and A. H. Zewail, Chem. Phys. Lett. **164**, 463 (1989).
[13] M. Drabbles, C. G. Morgan, D. S. McGuire, and A. M. Wodtke, J. Chem. Phys. **102**, 611 (1995).
[14] B.-C. Chang, M. Wu, G. E. Hall, and T. J. Sears (unpublished).
[15] I.-C. Chen and C. B. Moore, J. Phys. Chem. **94**, 263 (1990).
[16] E. R. Lovejoy, S. K. Kim, and C. B. Moore, Science **256**, 1541 (1992).
[17] E. R. Lovejoy and C. B. Moore, J. Chem. Phys. **98**, 7846 (1993).
[18] S. K. Kim, E. R. Lovejoy, and C. B. Moore, J. Chem. Phys. **102**, 3202 (1995).
[19] S. Yamabe and K. Morokuma, J. Am. Chem. Soc. **100**, 7551 (1978).
[20] W. D. Allen and H. F. Schaefer III, J. Chem. Phys. **84**, 2212 (1986).
[21] W. D. Allen and H. F. Schaefer III, J. Chem. Phys. **89**, 329 (1988).
[22] S. J. Klippenstein and R. A. Marcus, J. Chem. Phys. **91**, 2280 (1989).
[23] S. J. Klippenstein and R. A. Marcus, J. Chem. Phys. **93**, 2418 (1990).
[24] J. Yu and S. J. Klippenstein, J. Phys. Chem. **95**, 9882 (1991).
[25] P. Pechukas and J. C. Light, J. Chem. Phys. **42**, 3281 (1965); P. Pechukas, R. Rankin, and J. C. Light, J. Chem. Phys. **44**, 794 (1966); E. E. Nikitin, Teor i Eksperim. Khim. Acad. Nauk Ukr. SSR **1**, 135, 428 (1965); C. E. Klots, J. Phys. Chem. **75**, 1526 (1971).
[26] R. A. Marcus, Chem. Phys. Lett. **144**, 208 (1988).
[27] A. L. L. East, W. D. Allen, and S. J. Klippenstein, J. Chem. Phys. **102**, 8506 (1995).
[28] S. J. Klippenstein, A. L. L. East, and W. D. Allen, J. Chem. Phys. **101**, 9198 (1994).
[29] A. Szabo and N. S. Ostlund, *Modern Quantum Chemistry: Introduction to Advanced Electronic Structure Theory* (McGraw-Hill, New York, 1982).
[30] W. J. Hehre, L. Radom, P. v. R. Schleyer, and J. A. Pople, *Ab Initio Molecular Orbital Theory* (Wiley-Interscience, New York, 1986).
[31] C. Møller and M. S. Plesset, Phys. Rev. **46**, 618 (1934).
[32] J. A. Pople, J. S. Binkley, and R. Seeger, Int. J. Quant. Chem. Symp. **10**, 1 (1976).
[33] R. Krishnan and J. A. Pople, Int. J. Quant. Chem. **14**, 91 (1978).
[34] R. Krishnan, M. J. Frisch, and J. A. Pople, J. Chem. Phys. **72**, 4244 (1980).
[35] R. J. Bartlett, Annu. Rev. Phys. Chem. **32**, 359 (1981).
[36] G. D. Purvis and R. J. Bartlett, J. Chem. Phys. **76**, 1910 (1982).
[37] J. Paldus, in *New Horizons of Quantum Chemistry*, edited by P.-O. Löwdin and B. Pullman (Reidel, Dordrecht, 1983), p. 31.
[38] R. J. Bartlett, C. E. Dykstra, and J. Paldus, in *Advanced Theories and Computational Approaches to the Electronic Structure of Molecules*, edited by C. E. Dykstra (Reidel, Dordrecht, 1984), p. 127.
[39] G. E. Scuseria, A. C. Scheiner, T. J. Lee, J. E. Rice, and H. F. Schaefer III, J. Chem. Phys. **86**, 2881 (1987).
[40] A. C. Scheiner, G. E. Scuseria, J. E. Rice, T. J. Lee, and H. F. Schaefer III, J. Chem. Phys. **87**, 5361 (1987).
[41] K. Raghavachari, G. W. Trucks, J. A. Pople, and M. Head-Gordon, Chem. Phys. Lett. **157**, 479 (1989).
[42] G. E. Scuseria and T. J. Lee, J. Chem. Phys. **93**, 5851 (1990).
[43] N. C. Handy, J. A. Pople, M. Head-Gordon, K. Raghavachari, and G. W. Trucks, Chem. Phys. Lett. **164**, 185 (1989).
[44] K. Raghavachari, J. A. Pople, E. S. Replogle, and M. Head-Gordon, J. Phys. Chem. **94**, 5579 (1990).
[45] T. J. Lee, R. Kobayashi, N. C. Handy, and R. D. Amos, J. Chem. Phys. **96**, 8931 (1992).
[46] C. C. J. Roothaan, Rev. Mod. Phys. **23**, 69 (1951).
[47] In particular, three core orbitals were excluded for each of the basis sets and methods employed here. Furthermore, three virtual orbitals were excluded for the calculations employing either of the QZ(x,y) sets, while no virtual orbitals were excluded from those employing the 6-31G* basis. In the [13s8p6d4f,8s6p4d] MP2 procedures several high-lying virtual orbitals with energies greater than 23 a.u. were kept unoccupied. The number of such orbitals attributable to the C, O, and H core regions was 18, 29, and 6, respectively.
[48] A. L. L. East and W. D. Allen, J. Chem. Phys. **99**, 4638 (1993).
[49] (a) B. D. Wladkowski, A. L. L. East, J. E. Mihalick, W. D. Allen, and J. I. Brauman, J. Chem. Phys. **100**, 2058 (1994); (b) B. D. Wladkowski, W. D. Allen, and J. I. Brauman, J. Phys. Chem. **98**, 13532 (1994); (c) W. D. Allen, A. L. L. East, and A. G. Császár, in *Structures and Conformations of Non-Rigid Molecules*, edited by J. Laane, M. Dakkouri, B. van der Veken, and H. Oberhammer (Kluwer, Dordrecht, 1993), pp. 343–373; (d) A. L. L. East, C. S. Johnson, and W. D. Allen, J. Chem. Phys. **98**, 1299 (1993).
[50] *PSI 2.0* (PSITECH Inc., Watkinsville, Georgia, 1991).
[51] M. J. Frisch *et al.*, GAUSSIAN 92, Revision A, (Gaussian Inc., Pittsburgh, 1992).
[52] P. C. Hariharan and J. A. Pople, Theor. Chim. Acta. **28**, 213 (1973).
[53] S. Huzinaga, J. Chem. Phys. **42**, 1293 (1965).
[54] T. H. Dunning, Jr., J. Chem. Phys. **55**, 716 (1971).
[55] W. D. Allen and H. F. Schaefer III, Chem. Phys. **108**, 243 (1986).
[56] T. H. Dunning, Jr., J. Chem. Phys. **90**, 1007 (1989).
[57] F. B. van Duijneveldt, IBM Res. Rep. No. RJ 945 (IBM Research Laboratories, San Jose, 1971).
[58] J. Almlöf and P. R. Taylor, J. Chem. Phys. **86**, 4070 (1987).
[59] T. J. Lee and P. R. Taylor, Int. J. Quant. Chem. Symp. **23**, 199 (1989).
[60] H. R. Johnson and M. W. P. Strandberg, J. Chem. Phys. **20**, 687 (1952).
[61] J. S. Muenter, J. Mol. Spectrosc. **55**, 490 (1975).
[62] G. E. Scuseria, M. D. Miller, F. Jensen, and J. Geertsen, J. Chem. Phys. **94**, 6660 (1991); L. A. Barnes, B. Liu, and R. Lindh, J. Chem. Phys. **98**, 3972 (1993), and references therein.
[63] A. P. Rendell and T. J. Lee, J. Chem. Phys. **94**, 6219 (1991); T. J. Lee and A. P. Rendell, J. Chem. Phys. **94**, 6229 (1991).
[64] W. D. Allen and A. G. Császár, J. Chem. Phys. **98**, 2983 (1993).
[65] R. B. Woodward and R. Hoffmann, *The Conservation of Orbital Symmetry* (Academic, New York, 1970).
[66] *Orbital Symmetry Papers*, edited by H. E. Simmons and J. F. Bunnet (ACS Reprint Collection, American Chemical Society, Washington, D.C., 1974).
[67] D. A. Clabo, Jr., W. D. Allen, R. B. Remington, Y. Yamaguchi, and H. F. Schaefer III, Chem. Phys. **123**, 187 (1988).
[68] K. P. Huber and G. Herzberg, *Constants of Diatomic Molecules* (Van Nostrand, Princeton, 1979).
[69] J. R. Thomas, B. J. DeLeeuw, G. Vacek, T. D. Crawford, Y. Yamaguchi, and H. F. Schaefer III, J. Chem. Phys. **99**, 403 (1993).
[70] Near the bifurcation point the degree of nondynamical electron correlation may be substantial, and multireference *ab initio* methods may be necessary if a definitive mapping of this region is later required.
[71] The optimal alignment of dipoles at large distances gives a leading term of $-2\mu_{CO}\mu_{CH_2}/R^3$ for the electrostatic interaction energy (W). With $\mu_{CO}=0.114$ D (0.0449 a.u.) and $\mu_{CH_2}=1.752$ D (0.699 a.u.), one obtains W (cm^{-1})$=-2013/[R$ (Å)$]^3$. The interfragment separation R should be equated to $R_{CO}+b$ where b is between 0.5 and 1.0 Å from an appropriate quadrupole analysis (see Ref. 49a). Thus, at $R_{CO}=3.1$ Å, assuming $b=0.5$ Å, W is -43 cm^{-1}. The actual binding energy (Table V) at $R_{CO}=3.1$ Å is roughly a factor of 20 greater.
[72] K. Janowski, R. Bechere, P. Scharf, H. Schiffer, and R. Ahlrichs, J. Chem. Phys. **82**, 1413 (1985); R. Ahlrichs, P. Scharf, and K. Jankowski, Chem. Phys. Lett. **98**, 381 (1985); R. Becherer and R. Ahlrichs, Chem. Phys. **99**, 389 (1985).
[73] The 6-31G*→QZ(2d,2p) augmentation is only an apparent counterexample because a threshold of basis set completeness is frequently required for characteristic fp convergence properties, a level not reached by the modest 6-31G* set.
[74] V. J. Barclay, I. P. Hamilton, and P. Jensen, J. Chem. Phys. **99**, 9709 (1993).
[75] See also C. W. Bauschlicher, Jr. and H. Partridge, J. Chem. Phys. **100**, 4329 (1994) and references therein for benchmark studies on the dissociation energy of N_2.
[76] P. Ho and C. F. Melius, J. Phys. Chem. **94**, 5120 (1990); P. Ho, M. E. Coltrin, J. S. Binkley, and C. F. Melius, J. Phys. Chem. **89**, 4647 (1985); *ibid*. **90**, 3399 (1986); C. F. Melius, in *Springer-Verlag DFVLR Lecture Notes* (Springer, Berlin, 1990).
[77] D. Feldman, K. Meier, R. Schmiedl, K. H. Welge, Chem. Phys. Lett. **60**, 30 (1978); H. Petek, D. J. Nesbitt, C. B. Moore, F. W. Birss, D. A. Ramsay, J. Chem. Phys. **86**, 1189 (1987); H. Petek, D. J. Nesbitt, P. R. Ogilby, C. B. Moore, J. Phys. Chem. **87**, 5367 (1983); P. Jensen and P. R. Bunker, J. Chem. Phys. **89**, 1327 (1988); H. Petek, D. J. Nesbitt, D. C. Darwin, and C. B. Moore, J. Chem. Phys. **86**, 1172 (1987); H. Petek, D. J. Nesbitt, D. C. Darwin, P. R. Ogilby, C. B. Moore, and D. A. Ramsay, J. Chem. Phys. **91**, 6566 (1989); W. Xie, C. Harkin, H.-L. Dai, W. H. Green, Jr., Q. K. Zheng, and A. J. Mahoney, J. Mol. Spectrosc. **138**, 596 (1989); W. Xie, C. Harkin, and H.-L. Dai, J. Chem. Phys. **93**, 4615 (1990); G. V. Hartland, D. Qin, and H.-L. Dai, J. Chem. Phys. **98**, 2469 (1993).

[78] W. H. Green, Jr., N. C. Handy, P. J. Knowles, and S. Carter, J. Chem. Phys. **94**, 118 (1991).
[79] The vibrational procedure implemented for Table VII was invoked primarily for interpretive purposes and is distinct from the reduced dimensionality analyses in Sec. IV to determine vibrational energy levels in the conserved-mode space for varying reaction coordinates. Specifically, the method entailed a standard FG matrix analysis (Ref. 83) in the reduced internal space whereby the coordinates S_1-S_9 of Table VI were utilized and the force constants F_{41}, F_{42}, F_{43}, F_{54}, and F_{64} were set to zero, leaving F_{44} and all **G** matrix elements unaltered. Hence, the potential but not the kinetic energy coupling to the reaction coordinate was removed. Nonetheless, the effect of the potential coupling is small, never exceeding 3 cm^{-1} for the orthogonal modes except in the case of ω_5, which is downshifted by 5–30 cm^{-1}. The analogous shifts in the effective ω_4 values are $+25i$, $+9i$, $+4i$, and $+2i$, respectively, for R_{CC}=2.2, 2.5, 2.8, and 3.1 Å.
[80] The effect of the semidiagonal cubic force constants in each local representation is actually very small in the relaxation of the geometric structures. If terms only second order are included in the force field, the relaxed coordinates for the conserved modes change less than 0.0001 Å or 0.01°, R_{CC} is shifted less than 0.0011 Å, and the fragment orientation angles (δ,γ) vary no more than 0.5°. The concomitant effect on the relaxation energy (ΔE_{rlx}) is less than 3.1 cm^{-1} in all cases. These observations lend compelling numerical evidence as to the credibility of the local potential representations employed in the $R_{CO}\rightarrow R_{COM}$ transformations.
[81] INTDER is a general program developed by W. D. Allen and co-workers which performs vibrational analyses and higher-order nonlinear transformations among force field representations.
[82] S. J. Klippenstein, Chem. Phys. Lett. **214**, 418 (1993).
[83] E. B. Wilson, Jr., J. C. Decius, and P. C. Cross, *Molecular Vibrations* (Dover, New York, 1955).
[84] Maximum variations of 15, 7, 4, and 2 cm^{-1} were observed between the frequencies evaluated for the bond-length framework in the conserved-mode and conserved- plus transitional-mode spaces at R_{CC} values of 2.2, 2.5, 2.8 and 3.1 Å, respectively.
[85] S. J. Klippenstein in *Advances in Physical Chemistry: The Chemical Dynamics and Kinetics of Small Radicals*, edited K. Liu and A. F. Wagner (World Scientific, Singapore, 1996).
[86] While there is likely also some dependence of the conserved-mode force constants on the orientational coordinates, the latter dependence is expected to be negligible, particularly since these force constants are found to have only a minor variation along the reaction path (c.f., Table VI). Thus, for simplicity, the force constants for the R_{CC}-dependent optimized structures have been employed for all orientations at a given R_{CC} value.
[87] S. J. Klippenstein, J. Phys. Chem. **98**, 11459 (1994).
[88] S. J. Klippenstein, Chem. Phys. Lett. **170**, 71 (1990); S. J. Klippenstein, J. Chem. Phys. **94**, 6469 (1991); **96**, 367 (1992).
[89] S. J. Klippenstein and R. A. Marcus, J. Chem. Phys. **87**, 3410 (1987).
[90] S. J. Klippenstein (unpublished).
[91] This second approach is essentially equivalent to that employed in our preliminary report of this work (Ref. 28), where the conserved-mode frequencies were obtained via a projection of the reaction coordinate from the force constant matrix, specifically setting the off-diagonal coupling to the reaction coordinate to zero [D.-H. Lu and D. G. Truhlar, J. Chem. Phys. **99**, 2723 (1993); W. H. Miller, N. C. Handy, and J. E. Adams, J. Chem. Phys. **72**, 99 (1980)]. However, the use of the reduced *G* matrix is more appropriate for the present situation. The additional consideration of the COM reaction coordinate framework here leads to results which overall are nearly identical to those previously reported.
[92] D. Papoušek and M. R. Aliev, *Molecular Vibrational-Rotational Spectra* (Elsevier, Amsterdam, 1982). The E_0 term described in D. G. Truhlar and A. D. Isaacson, J. Chem. Phys. **94**, 357 (1991) is negligible at the energies of interest here and has been neglected.
[93] See, e.g., R. H. Clarke and H. A. Frank, J. Chem. Phys. **65**, 39 (1976); R. H. Clarke and J.-M. Hayes, Chem. Phys. Lett. **27**, 556 (1974); D. A. Anthenius, J. Schmidt, and J. H. van der Waals, Mol. Phys. **27**, 1521 (1974); M. A. El-Sayed, W. R. Moomaw, and J. B. Chodak, Chem. Phys. Lett. **20**, 11 (1973); F. Metz, Chem. Phys. Lett. **22**, 186 (1973).
[94] S. A. Reid and H. Reisler, J. Chem. Phys. **101**, 5683 (1994); S. Ionov, H. F. Davis, K. Mikhaylichenko, L. Valachovic, R. A. Beaudet, and C. Wittig, J. Chem. Phys. **101**, 4809 (1994); and references cited therein.
[95] J. O. Hirschfelder and E. Wigner, J. Chem. Phys. **7**, 616 (1939); W. H. Miller, J. Chem. Phys. **65**, 2216 (1976); W. J. Chesnavich, L. Bass, T. Su, and M. T. Bowers, J. Chem. Phys. **74**, 2228 (1981).
[96] See, for example, J. C. Corchado, J. Espinosa-Garcia, W.-P. Hu, I. Rossi, and D. G. Truhlar, J. Phys. Chem. **99**, 687 (1995) for a related combination of high-level and low-level *ab initio* data along the reaction path.
[97] B. Ma, R. A. King, W. D. Allen, and H. F. Schaefer (unpublished).
[98] See N. E. Klepeis, A. L. L. East, A. G. Császár, W. D. Allen, T. J. Lee, and D. W. Schwenke, J. Chem. Phys. **99**, 3865 (1993) for a triatomic comparison of various state counts at high vibrational energies.
[99] S. J. Klippenstein, J. Chem. Phys. **101**, 1996 (1994).